Artificial Intelligence in Agriculture 16 (2026) 206–223

Contents lists available at ScienceDirect

Artificial Intelligence in Agriculture

journal homepage: http://www.keaipublishing.com/en/journals/artificial-intelligence-in-agriculture/

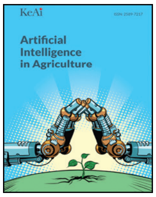

Research Paper

Inversion of plant functional traits from hyperspectral imagery enhances the distinction of wheat stripe rust severity

Kehui Ren [a,b], Anting Guo [a], Binxiang Qian [a,b], Chao Ruan [c], Wenjiang Huang [a,b,d,*], Yingying Dong [a,b,d], Xia Jing [e], Kun Wang [a,b,d], Tiecheng Huang [f], Huiqin Ma [g]

[a] Key Laboratory of Remote Sensing and Digital Earth, Aerospace Information Research Institute, Chinese Academy of Sciences, Beijing 100101, China
[b] University of Chinese Academy of Sciences, Beijing 100049, China
[c] National Engineering Research Center for Agro-Ecological Big Data Analysis and Application, Anhui University, Hefei 230601, China
[d] Sino-UK Pest and Disease Forecasting & Management Joint Laboratory, Beijing 100101, China
[e] College of Geometrics, Xi'an University of Science and Technology, Xi'an 710054, China
[f] College of Forestry and Landscape Architecture, Xinjiang Agricultural University, Urumqi 830052, China
[g] School of Automation, Hangzhou Dianzi University, Hangzhou 310018, China

ARTICLE INFO

Article history:
Received 11 April 2025
Received in revised form 16 October 2025
Accepted 19 October 2025
Available online 26 October 2025

Keywords:
Stripe rust
UAV hyperspectral
PROSAIL
Plant functional traits
Hybrid inversion model

ABSTRACT

Wheat stripe rust can cause yield losses of up to 40 % during severe outbreaks, underscoring the importance of timely and accurate detection for effective management. Traditional hyperspectral methods relying on vegetation indices (VIs) and texture features (TFs) offer indirect assessments prone to environmental interference. In contrast, plant functional traits (PTs) supply a more consistent and informative reflection of stress progression. Accurately quantifying PTs, alongside traditional VIs and TFs, is therefore essential for constructing a comprehensive and robust disease monitoring framework. First, this study utilized correlation coefficient analysis and variance inflation factor (VIF) analysis to filter conventional variables (VIs and TFs) from candidate feature sets. The hybrid inversion model (HIM) was then employed to retrieve critical PTs—CCC, Car, Anth, CBC, and LAI—from UAV hyperspectral data, while canopy temperature (T_c) was derived from thermal imagery. Subsequently, 28 disease monitoring models were developed using machine learning algorithms (RF, AdaBoost, GBRT, and LASSO), incorporating both individual and combined features. Model performance was rigorously assessed through 6-fold cross-validation. The results demonstrated that PTs significantly responded to wheat rust disease ($p\text{-value} < 0.001$), manifesting as reductions in pigment content (CCC, Car, Anth) and structural parameters (LAI), along with increases in CBC and T_c. During model development, PTs exhibited superior performance over VIs and TFs, given their strong association with plant health and sensitivity to biotic stress. Moreover, the sparsity of LASSO, combined with synergistic integration of multiple feature types, substantially enhanced model accuracy. The optimal model, integrating all three feature categories via LASSO regression, yielded R^2, RMSE, and MAE values of 0.628, 8.03 %, and 6.57 %, respectively. Overall, this study advances the accuracy of wheat stripe rust monitoring by integrating PTs, VIs, and TFs to create a physiological-spectral–morphological synergy, providing valuable insights for large-scale disease detection on airborne and satellite platforms.

1. Introduction

Wheat, as the dominant cereal crop globally, is a crucial source of calories and plant-based protein for humans. The loss of resistance in major cultivars, favorable rainfall conditions, and human activities have made stripe rust one of the primary threats to wheat production. In years of severe outbreaks, it can cause yield losses reaching 40 % or even complete crop failure. Traditional methods, such as visual inspections and field sampling, are time-intensive and laborious, making them impractical for the efficient and precise management of crop diseases.

In recent years, with the rapid advancement of sensor technologies and signal processing methods, remote sensing offers a scalable and non-invasive solution for crop disease detection. Compared to ground-based and satellite platforms, airborne platforms offer greater flexibility and are less constrained by revisit cycles and weather conditions (Wang et al., 2024a). By integrating sensors spanning the electromagnetic spectrum (including RGB, multispectral, hyperspectral, and thermal

---

* Corresponding author at: Aerospace Information Research Institute, Chinese Academy of Sciences, No.9 Dengzhuang South Road, Haidian District, Beijing 100094, China.
E-mail address: huangwj@aircas.ac.cn (W. Huang).

https://doi.org/10.1016/j.aiia.2025.10.006

infrared), airborne platforms furnish an in-situ alternative for capturing and quantifying vegetation stress levels (Zhang et al., 2023). Among these, hyperspectral sensors, characterized by narrower bandwidths across continuous spectral ranges, allow for a more precise depiction of crop absorption and reflection variations at different wavelengths during disease infection (Shuai et al., 2024).

Sensitive features extensively applied in plant disease research primarily include spectral features and phenotypic traits. Depending on the processing approach utilized for raw spectra, spectral features can be further categorized into reflectance bands, vegetation indices, and derived features (e.g., wavelet features and fractional-order derivative features), all of which have been proven effective in disease stress monitoring. For instance, Xiao et al. (2022) adopted the minimum redundancy maximum relevance (mRMR) algorithm to select the Ratio Vegetation Index (RVI), Anthocyanin Reflectance Index (ARI), and Triangular Vegetation Index (TVI), then leveraged the Random Forest (RF) algorithm to develop an apple fire blight detection model with an accuracy of 94.0 %. Tian et al. (2021) observed four continuous wavelet features (WFs) in the near-infrared region (750–1000 nm) that displayed strong separability between diseased and healthy rice leaves, considerably facilitating the detection of subtle disease signals. In numerous studies, phenotypic traits (such as texture, color, and size) have markedly enhanced disease detection and identification accuracy through synergistic modeling with traditional spectral features (Liu et al., 2024). Ma et al. (2024) investigated the effectiveness of integrating vegetation indices, color indices, and texture features for monitoring cotton verticillium wilt severity. The results indicated that the fusion of all three data sources outperformed any single source or pairwise combination. However, in Gray-Level Co-occurrence Matrix (GLCM)-based texture feature extraction, window size influences the trade-off between local details and global information (Guan et al., 2020). Selecting an appropriate window size is crucial for accurately capturing the spatial aggregation pattern of disease. Xiao et al. (2021) found that the optimal window size for Fusarium Head Blight (FHB) detection in wheat varied across different key developmental stages due to differences in host conditions and disease distribution. Nevertheless, vegetation indices are constrained by a limited spectral range and frequently overlook subtle physiological variations in early infection stages. Likewise, texture features indicate structural heterogeneity but serve as indirect and lagging proxies of plant health. These limitations highlight the necessity for physiologically relevant traits such as PTs.

PTs, such as canopy temperature, dry matter content, biochemical composition, vegetation structure, and solar-induced chlorophyll fluorescence (SIF), are closely associated with vegetation health and stress responses (Hornero et al., 2021). Consequently, their application in disease monitoring has been steadily expanding. With increasing stress, key parameters such as leaf pigment content and canopy structure undergo substantial alterations, making their robust quantification critical for developing scalable and effective stress detection strategies (Berger et al., 2022). Compared to healthy vegetation, stressed plants typically exhibit elevated canopy temperature and dry matter content, along with reductions in PTs such as pigment concentration, leaf area index (LAI), water content, and SIF (Camino et al., 2021). Several researchers have employed airborne platforms to acquire thermal infrared and multi/hyperspectral imagery for the early detection and monitoring of forest diseases. For instance, Hornero et al. (2024) proved that combining multispectral and thermal infrared data effectively classified oak tree decline, achieving performance comparable to hyperspectral imagery alone. However, relying solely on multispectral or thermal infrared data was insufficient for accurately assessing disease severity. In a similar vein, Smigaj et al. (2019) utilized drone-based thermal imaging to detect canopy temperature increases induced by needle blight and identified a notable statistical correlation between temperature variations and disease severity, likely associated with needle damage symptoms. Furthermore, retrieving functional PTs, such as chlorophyll, carotenoid, and dry matter content, from hyperspectral data has been shown to enhance plant disease monitoring. For example, Watt et al. (2023) markedly improved the prediction accuracy of needle blight severity in radiata pine by integrating five inverted PTs into a narrowband hyperspectral index (NBHI), yielding an R^2 of 0.85. Zarco-Tejada et al. (2018) demonstrated that PTs retrieved from airborne imaging spectroscopy and thermal imaging could reveal xylem bacterial infections in olive trees before symptom onset, with a precision exceeding 80 %.

Inverse modeling is essential for the reliable quantification of PTs. Traditional methods rely on empirical statistical relationships between PTs and spectra to construct simple linear, polynomial, exponential, or logarithmic models (Adeluyi et al., 2021). Although these methods are straightforward and convenient, their empirical relationships are highly susceptible to external factors, such as sensor characteristics and vegetation type (Chakhvashvili et al., 2022). Mechanistic models, such as radiative transfer models (RTM), which are built on rigorous theoretical foundations and physical principles, quantitatively describe the interaction between canopy structure parameters and reflectance, remaining unaffected by factors like vegetation type (Wan et al., 2021). Currently, RTM-based PTs inversion methods are broadly categorized into two approaches (Sahoo et al., 2024): (i) Look-up tables (LUT), which associate simulated spectra with measured parameters via cost functions; however, this method entails high storage and computational costs and poses challenges in determining the optimal cost function (Zhu et al., 2023); and (ii) hybrid inversion models (HIMs), which integrate the simplicity of empirical statistical approaches with the mechanistic rigor and generalizability of physical models (Li et al., 2024). HIMs fundamentally rely on constructing a database of simulated spectra and corresponding PTs derived from RTM, followed by leveraging machine learning algorithms (parametric or non-parametric regression models) to elucidate their underlying relationships.

Despite the growing use of RTM-based plant trait inversion in forestry disease studies (Hornero et al., 2020; Poblete et al., 2023), it remains unclear whether such traits offer superior discriminatory power over conventional spectral and phenotypic indicators in crop disease scenarios. Moreover, few studies have investigated integrated modeling approaches, resulting in a lack of systematic evaluation of the relative performance among the three feature types, as well as limited conclusive evidence supporting their potential synergistic effects in monitoring wheat stripe rust. Therefore, this study focuses on applying HIMs to retrieve functional PTs from UAV hyperspectral imagery of wheat. These PTs are then integrated with selected VIs and TFs to develop stripe rust disease monitoring models using multiple algorithms, including RF, AdaBoost, GBRT, and LASSO. The specific objectives are: (i) to evaluate the capability of inverted PTs in distinguishing different severity levels of wheat stripe rust and determining the relative importance of each indicator; (ii) to investigate whether the synergy of multi-source features enhances model performance; and (iii) to compare the performance of different machine learning algorithms and identify the most suitable model based on the optimal feature combination.

2. Materials and methods

2.1. Study area

The field experiment was conducted from April 26 to 28, 2024, in Xiakouyi Town, Lueyang County, Shaanxi Province, China (33°10′36″N, 106°24′5″E). The study area lies on the southern slopes of the Qinling Mountains, featuring a landscape primarily composed of alpine valleys and river plains (Fig. 1a). It has a subtropical monsoon humid climate, with an annual average temperature of 12 °C and approximately 970 mm of annual precipitation. The dominant soil type in the region is yellow-brown earth. The study site is part of the Southwest Winter Wheat Zone, a rice-wheat rotation region, and serves as a key overwintering inoculum reservoir sustaining the epidemic cycle of wheat stripe rust in China. The experimental field spans approximately

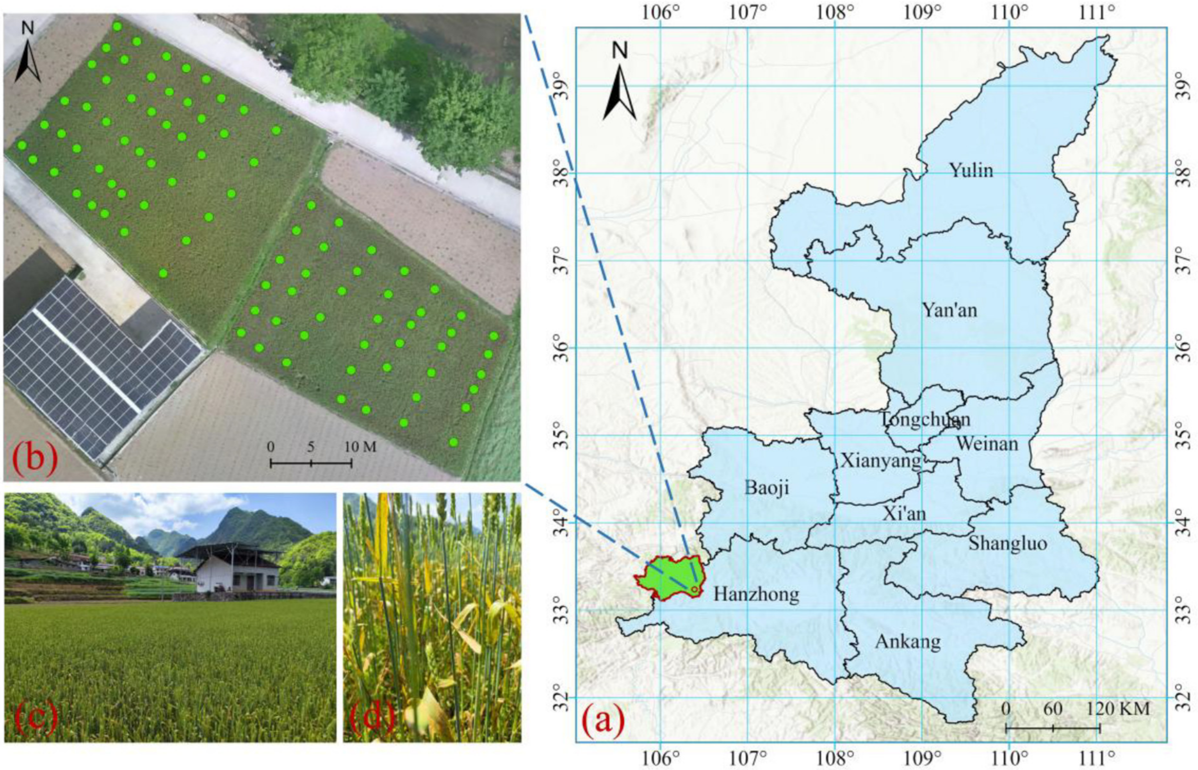

Fig. 1. Location of the study area.

1250 m^2, with 'Mianyang 19', a stripe rust-susceptible wheat cultivar. The crop was sown on October 20, 2023, and managed by local farmers following standard agronomic practices without fungicide application, allowing for natural stripe rust infection throughout the growing season.

2.2. Disease index assessment

The experimental field was divided into 90 elementary sampling units (ESU), each a square plot measuring approximately 60 cm per side, evenly distributed across the study area (Fig. 1b). In this study, wheat stripe rust severity was quantified based on the disease index (DI). In each ESU, five symmetrical sampling points were selected along the diagonal. At each point, two wheat plants were randomly destructively sampled, and disease severity was assessed using the top five leaves from each selected plant, following the Technical Specification for Wheat Stripe Rust Monitoring and Forecasting (GB/T 15795–2011). The proportion of lesion-covered area on diseased leaves, relative to the total leaf area, was classified into eight severity levels: 1 %, 5 %, 10 %, 20 %, 40 %, 60 %, 80 %, and 100 %, mapped to corresponding disease grades from 1 to 8. The number of leaves at each severity level was recorded, and the overall disease severity for each sampling plot was quantified following Eq. (1).

$$DI = \sum (x \cdot f)/(n \cdot \sum f) \tag{1}$$

In the equation, DI represents the disease index, x denotes the value of each grade, n is the highest grade, and f refers to the number of leaves corresponding to each grade.

2.3. Data collection and processing

Fig. 2 illustrates the technical workflow of this study, which primarily covers data collection and processing, feature extraction and optimization, as well as model construction and comparison.

2.3.1. Field data measurement

On April 26, 2024, under stable and sufficient midday sunlight, in situ LAI measurements were obtained with the SunScan Canopy Analysis System (Delta-T Devices Limited, Cambridge, U.K.). Equipped with a Beam Fraction Sensor, SunScan Probe, and Personal Digital Assistant, the SunScan system determines LAI by quantifying the photosynthetically active radiation (PAR) intercepted by the canopy (Cotter et al., 2017). To minimize experimental uncertainty, wheat was measured at three orientations (0°, 60°, and 120° relative to the sowing row direction) within each ESU, and the mean value of these observations was computed to derive LAI$_{mea}$. Additionally, chlorophyll content and nitrogen balance index (NBI) were assessed using the SPAD-502 (Konica Minolta, Tokyo, Japan) and Dualex Scientific (Force-A, Orsay, France), respectively. Within each ESU, three wheat plants were randomly selected, and SPAD values were sequentially recorded from top to bottom for all leaves, with the mean value calculated as SPAD$_{mea}$. SPAD$_{mea}$ is a dimensionless parameter strongly correlated with the leaf chlorophyll content (LCC) and was converted to LCC$_{mea}$ (μg/cm^2) using Eq. (2) (Guo et al., 2024b).

$$LCC_{mea} = 9.1411e^{0.00318*SPAD_{mea}} \tag{2}$$

Similar to the SPAD-502, the Dualex Scientific is a leaf-clip sensor that estimates leaf chlorophyll absorption by comparing the transmittance difference between two near-infrared wavelengths (710 nm and 850 nm) (Gabriel et al., 2017). In this study, this parameter is denoted as Chl. Additionally, the device measures the maximum absorption of flavonoids (Flav) using a 357 nm ultraviolet excitation beam (Vatter et al., 2024). The NBI is defined as the ratio of Chl to Flav, providing an indicator for assessing crop nitrogen status under stress conditions (Raya-Sereno et al., 2024). For each ESU, three wheat plants were randomly selected, with two repeated Dualex measurements performed on each plant. The mean values from six measurements of Chl and NBI were calculated to obtain the final ESU-level values.

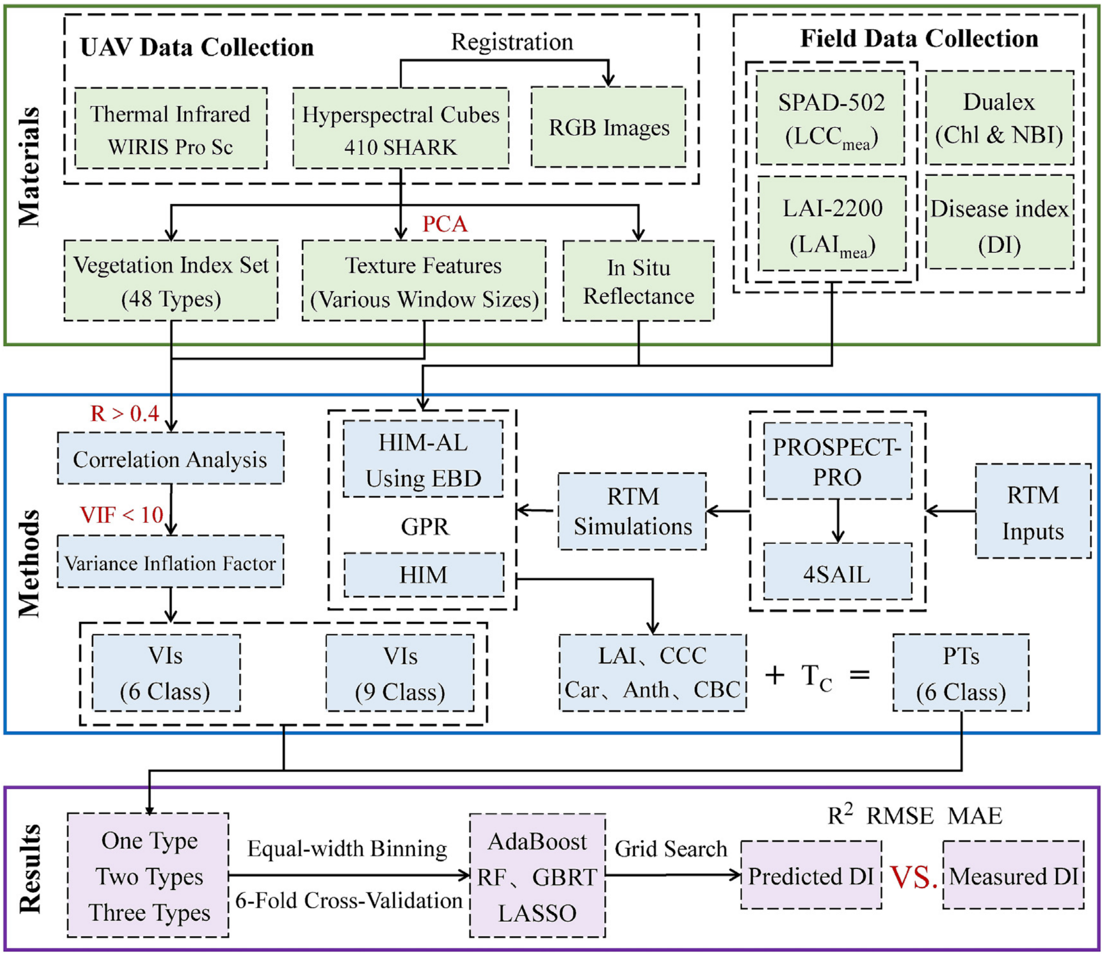

Fig. 2. Workflow for constructing monitoring models in this study.

2.3.2. UAV image acquisition

Airborne hyperspectral data were acquired on April 28, 2024, from 11:15 to 11:45 (UTC +8) under clear, windless, and cloud-free conditions. The study area was imaged with a Corning® microHSI™ 410 SHARK camera mounted on a Matrice 350 RTK UAV (DJI Technology Co., Ltd., Shenzhen, China). This push-broom hyperspectral sensor operates within the 400–1000 nm spectral range, with a full width at half maximum (FWHM) of 5 nm. It captures 150 spectral bands with 682 spatial pixels and features a 16 mm focal length, a 29.5° field of view (FOV, 515 mrad), and an instantaneous field of view (IFOV) of 366 μrad. During data acquisition, the UAV was programmed to operate at an altitude of 40 m and a speed of 4.68 m/s, with forward and side overlaps set to 77 % and 30 %, respectively, resulting in a ground sample distance (GSD) of 3.01 cm. The sensor utilizes a linear arrangement of multiple optical detectors to spatially record incoming light passing through a prism (Kwon et al., 2022). To ensure sufficient sampling and prevent data gaps, the sensor operated at a frame rate of 160 Hz with an integration time of 6 ms. Additionally, images were stored in both raw DN values and radiance format (units: $W/m^2/sr/\mu m$), with each acquisition corresponding to a continuous hyperspectral strip (Singh et al., 2021).

This study deployed the WIRIS Pro Sc thermal imager (Workswell, Prague, Czech Republic), which was likewise mounted on the Matrice 350 RTK. The thermal imager exhibits a temperature sensitivity of 30 mK, a resolution of 640 × 512 pixels, and a spectral range covering 7.5–13.5 μm. It acquires imagery in TIFF radiometric format, providing accurate temperature recordings, with an emissivity set at 0.95. Additionally, the system incorporates an RGB camera with a resolution of 1920 × 1080 pixels. Thermal images were collected between 11:35 and 11:45 on April 26, 2024 (UTC +8), with the UAV operating at an altitude of 35 m and a speed of 2.70 m/s. The flight maintained 80 % forward and 70 % side overlap, yielding a GSD of 4.45 cm. Table 1 presents a comprehensive summary of the UAV hyperspectral and thermal infrared sensor specifications, along with the flight parameters.

2.3.3. Hyperspectral-thermal infrared data preprocessing

DI, agronomic parameters, and thermal infrared data were collected on April 26, 2024, with hyperspectral measurements obtained two days later due to logistical and weather constraints. Temperatures during this

Table 1
Summary of UAV flight and sensor parameters.

Parameters	UAV-Hyperspectral System	UAV-Thermal Infrared System
Sensor	410 SHARK	WIRIS Pro Sc
Acquisition date	28 Apr. 2024	26 Apr. 2024
Flight height (m)	40	35
Flight speed ($m \cdot s^{-1}$)	4.68	2.70
Forward overlap (%)	77	80
Side overlap (%)	30	70
Spatial resolution (cm)	3.01	4.45
Wavelength range	400–1000 nm	7.5–13.5 μm
Number of bands	150	1
FWHM (nm)	5.0	–
Temperature sensitivity (mK)	–	30

period exceeded the optimal range for stripe rust, minimizing disease progression. Thus, disease status remained stable, rendering the temporal gap negligible and preserving data consistency.

Following UAV flight and image acquisition, several preprocessing steps were performed using Metashape Professional 1.8.5 (Agisoft LLC, St. Petersburg, Russia) and ENVI 5.6 (Harris Geospatial Solutions, Boulder, U.S.). First, Metashape was employed to generate high-density point clouds, construct digital elevation models (DEM), and produce orthophotos from the RGB images acquired by the WIRIS Pro Sc. The creation of a geographic image covering the entire experimental area provided the necessary spatial reference for processing the hyperspectral strips. For thermal infrared data in TIFF format, in addition to the aforementioned processing steps, the DN values were further converted to degrees Celsius using the “Band Math” tool in ENVI, based on the factory calibration equation: float (b1) * 0.025–100. Owing to the high spatial resolution, low flight altitude, nadir viewing geometry, well-developed wheat canopy, and radiometric calibration applied, the retrieved thermal values can be considered a reliable approximation of the actual canopy temperature.

Due to its linear scanning mechanism, the data acquired by the 410 SHARK consist of a single continuous strip, which lacks geographic location information. Therefore, a sequence of steps, including image cropping, registration (referencing the RGB base map), mosaicking, and reflectance conversion, were conducted to generate a comprehensive hyperspectral image.

2.4. Spectral and image feature extraction and optimization

2.4.1. Vegetation indices

Wheat stripe rust predominantly affects the leaves, manifesting as orange-yellow, blister-like lesions arranged along the leaf veins. As the disease advances, the lesions progressively enlarge, causing leaf desiccation and necrosis, along with chlorosis, yellowing, disrupted photosynthesis, and physiological alterations, including water stress (Zhao and Kang, 2023). These biochemical and morphological changes lead to spectral alterations, while the physical foundation of vegetation indices is based on understanding the complex interactions between light and vegetation (Zeng et al., 2022), enabling effective detection of disease-induced stress. In this study, 48 vegetation indices associated with crop pigments, water content, and stress quantification were gathered from an extensive literature review as potential features for constructing a stripe rust disease monitoring model. Table S1 presents comprehensive details on the name, abbreviation, calculation formula, and source of each vegetation index.

2.4.2. Texture feature

As the disease develops, winter wheat plants display noticeable alterations in canopy structure. Texture features, which capture grayscale variations between adjacent pixels, improve the interpretability of plots across varying disease severity levels (Liu et al., 2024). The GLCM is extensively employed for texture extraction owing to its computational efficiency and its capability to discern multi-scale features across diverse orientations. In this study, eight commonly used TFs were selected, including Mean, Variance, Homogeneity, Contrast, Dissimilarity, Entropy, Second Moment, and Correlation. Table 2 lists the calculation equations for GLCM-based TFs.

The hyperspectral imagery captured by the 410 SHARK sensor comprises 150 bands, exhibiting substantial feature overlap and containing considerable redundant information. Therefore, dimensionality reduction was initially performed on the hyperspectral data using the PCA module in ENVI 5.6, yielding the first three principal component images (PC1, PC2, and PC3, with a cumulative variance of 94.5 %). Next, the GLCM tool in ENVI was implemented to extract TFs at multiple orientations (0°, 45°, 90°, and 135°) using sliding windows of various sizes (3 × 3, 5 × 5, …, 15 × 15, and 17 × 17). For example, feature extraction using a 3 × 3 window resulted in the creation of 24 TFs for the first three principal component images. To simplify the description, TFs are expressed by combining the feature abbreviation with the principal component number. For example, Mea1 represents the Mean feature corresponding to the PC1 component.

Table 2
The equation of texture used in this study.

Texture	Equation
Mean, MEA	$\mathrm{MEA} = \sum_{i,j} i \cdot p(i,j)$
Variance, VAR	$VAR = \sum_{i,j} (i-u)^2 p(i,j)$
Homogeneity, HOM	$HOM = \sum_{i,j} \frac{p(i,j)}{1+(i-j)^2}$
Contrast, CON	$CON = \sum_{i,j} (i-j)^2 p(i,j)$
Dissimilarity, DIS	$DIS = \sum_{i,j} \lvert i-j \rvert p(i,j)$
Entropy, ENT	$ENT = \sum_{i,j} p(i,j) log(p(i,j))$
Second moment, SEM	$SEM = \sum_{i,j} p(i,j)^2$
Correlation, COR	$COR = \sum_{i,j} (i-\mu_x)\left(j-\mu_y\right) p(i,j)/\sigma_x\sigma_y$

2.4.3. PTs inverted by hybrid inversion models

The HIMs employed for PTs retrieval is fundamentally based on a forward RTM to simulate spectra, as well as physiological and structural parameters. Subsequently, machine learning regression algorithms (MLRA) are utilized to construct the mapping between the simulated spectra and the corresponding parameters. Ultimately, the inversion model is applied to in-situ observed spectra, facilitating the retrieval of the target variables (Tagliabue et al., 2022).

(1) **Radiative transfer model**

In this study, the leaf-level RTM PROSPECT-PRO (Féret et al., 2021) and the canopy-level 4SAIL model (Verhoef and Bach, 2007), hereafter referred to as PROSAIL, were adopted to generate simulated spectra and corresponding PTs. The PROSPECT-PRO model incorporates eight leaf parameters: structure, chlorophyll, carotenoids, anthocyanins, brown pigments, equivalent water thickness, protein content, and carbon-based components, and provides leaf directional-hemispherical reflectance and transmittance over the spectral range of 400–2500 nm (with a spectral resolution of 1 nm). The 4SAIL model simulates the optical properties of plant canopies, with parameters such as LAI, leaf angle distribution, diffuse/direct radiation ratio, hotspot parameters, and solar-target-sensor geometry. The input parameters for the PROSAIL model were determined based on field measurements and relevant literature, as detailed in Table 3.

(2) **Inversion of non-measured PTs with GPR**

The optical properties of leaves are governed by their absorption and scattering characteristics, with the absorption of pigments such as chlorophyll, carotenoids, and anthocyanins being particularly pronounced in the visible light range (400–750 nm) (Qiu et al., 2018). Carbon-based components mainly influence the near-infrared and shortwave infrared regions, where leaf reflectance decreases as the carbon content increases (Lijuan and Zheng, 2014), which overlaps with the spectral bands detectable by the hyperspectral sensor 410 SHARK (750–1000 nm). However, the three primary absorption bands of leaf water fall within the range of 1350 to 2500 nm, making it impossible to retrieve relevant information from UAV-captured hyperspectral data. Therefore, for non-measured trait parameters, this study will focus on retrieving carotenoids, anthocyanins, and carbon-based components.

Following the settings in Table 3, a sampling approach based on the Probability Density Function (PDF) was employed to randomly generate a subset comprising 10,000 simulated spectra and corresponding PTs.

Table 3
Parameter settings for the PROSAIL model in this study.

Model	Parameters	Description	Unit	Range
PROSPECT-PRO (Leaf)	N	Leaf structure	Unitless	1–1.2
	C_{brown}	Brown pigment content	Unitless	0
	Anth	Leaf anthocyanin content	μg/cm^2	1–5
	Car	Leaf carotenoid content	μg/cm^2	2–15
	LCC	Leaf chlorophyll content	μg/cm^2	10–45
	EWT	Leaf water content	cm	0.001–0.02
	CBC	Carbon-based constituents	g/cm^2	0.001–0.015
	C_p	Leaf protein content	g/cm^2	0.0005–0.0015
4SAIL (Canopy)	LAI	Leaf area index	m^2/m^2	0.5–4.5
	HOT	Hot spot parameter	m/m	0.01
	ALA	Average leaf angle	deg	55–65
	SZA	Solar zenith angle	deg	23.5
	OZA	Observer zenith angle	deg	0
	RAA	Relative azimuth angle	deg	0
	FVC	Fractional vegetation cover	fraction	0.8
	Skyl	Diffuse solar radiation	fraction	0.05
	α_{soil}	Soil brightness	unitless	0.3

Then, the simulated reflectance was resampled according to the spectral bandwidth and response function of the 410 SHARK to match the measured hyperspectral data. This study utilizes Gaussian Process Regression (GPR), an algorithm whose effectiveness has been extensively validated in numerous similar studies (Pipia et al., 2021; Verrelst et al., 2021). GPR is a non-parametric probabilistic model grounded in Bayesian theory, capable of capturing complex nonlinear relationships through kernel functions, and exhibiting exceptional modeling performance, especially in small-sample scenarios. Furthermore, to mitigate band collinearity and reduce spectral information redundancy, principal component analysis (PCA) was applied to condense the 150 original bands into five principal components. The 10,000 simulated spectra and corresponding PTs were randomly divided into training (80 %) and testing (20 %) datasets to develop and evaluate the performance of the non-measured trait parameter HIMs. Finally, the optimal models were applied to estimate carotenoids, anthocyanins, and carbon-based components from the mean hyperspectral reflectance of 90 ESUs.

(3) **Empirical PTs inversion integrated with AL**

Based on the in-situ observed LAI_{mea} and LCC_{mea}, the conversion of chlorophyll content from the leaf level to the canopy level was achieved according to Eq. (3) (Guo et al., 2024b). CCC_{mea} was used to simulate the aboveground chlorophyll content, measured in g/m^2. In this study, the aforementioned three types of measured indicators are verifiable empirical PTs. By combining spectra and PTs simulated by the RTM, HIMs incorporating active learning (AL) can be established, which facilitate large-scale parameter inversion at the image level (Tagliabue et al., 2022; Verrelst et al., 2021). The primary focus is to investigate whether PTs inverted from in-situ observed spectra can enhance disease monitoring accuracy. Therefore, image mapping was not conducted for these parameters in this study.

$$CCC_{mea} = LCC_{mea} \times LAI_{mea}/100 \tag{3}$$

To mitigate the effect of sample size on retrieval model accuracy (Adeluyi et al., 2021), subsets of different sizes (1000, 1500, 2000, 2500, and 3000 samples) were randomly selected from the 10,000 simulated spectra and their corresponding PTs. For HIMs integrating AL, the quality of training data often surpasses its quantity. While a dataset of just a few thousand samples may appear limited, it is sufficient to achieve optimal performance (Berger et al., 2021). Additionally, the implementation of GPR necessitates the inversion of an N × N matrix, causing processing time to scale exponentially with increasing sample size, where N denotes the number of simulations (Verrelst et al., 2021).

Beyond applying PCA for spectral-domain dimensionality reduction by extracting five principal components, this study harnessed the heuristic iterative nature of AL to selectively identify and annotate the most informative samples, thereby improving model efficiency. The specific process is as follows: 20 spectra were randomly selected from the LUT to create the initial pool, with one sample added sequentially at each step according to the chosen AL criterion. New samples were retained if they improved model performance; otherwise, they were discarded. This iterative process continued until all simulations were evaluated. Studies have demonstrated that the Euclidean distance-based diversity (EBD) method offers distinct advantages in parameter retrieval. It selects simulations that are far from the existing training set samples by calculating the squared Euclidean distance (Eq. (4)). The HIMs for PTs retrieval were implemented in MATLAB R2024a (MathWorks, Natick, USA), utilizing the MLRA toolbox from ARTMO v.3.31 (https://artmotoolbox.com).

$$d_E = \|X_u - X_l\| \tag{4}$$

In the equation, X_u represents the sample from the candidate dataset, and X_l refers the sample from the training dataset. The distance between all the samples is calculated, and the sample with the farthest distance is selected.

2.4.4. Feature selection based on a two-step filtering method

Currently, there was an overabundance of vegetation indices and texture features, many of which exhibit weak disease-specific correlations with stripe rust. Directly incorporating these features into the modeling process without appropriate screening was likely to escalate computational complexity, diminish generalization ability, and hinder model interpretation (Lan et al., 2020).

Therefore, this study implemented a two-step filtering procedure to select a feature set that was most closely associated with stripe rust, while simultaneously minimizing redundancy among features. First, the correlation coefficient (R) between each vegetation index and texture feature with the DI was calculated individually. With a significance level of $\alpha = 0.001$, the critical R value was determined from the correlation coefficient table, where the remaining degrees of freedom $v = n - 2 = 88$, yielding a critical value of 0.325. The analysis above indicates that, at a 99.9 % confidence level, the correlation coefficient between a feature and DI must be no less than 0.325. To strengthen the filtering criteria, all features with a correlation coefficient lower than 0.40 were further excluded. Next, VIF analysis was performed separately for the VIs and the TFs. Features with the highest VIF values were iteratively removed until all VIF values fell below 10, thereby mitigating multicollinearity among the monitoring features, which could otherwise distort model estimates (Hornero et al., 2024). The VIF analysis was conducted using the procedure outlined in SPSS 27 (IBM Corporation, Armonk, USA).

2.5. Construction and evaluation of wheat stripe rust monitoring models

In this study, to assess whether inverted PTs and multi-source feature synergy could enhance the accuracy of wheat stripe rust disease monitoring, the model variables were classified into seven categories: single data sources (VIs, TFs, and PTs) and multi-source combinations (VIs + TFs, VIs + PTs, TFs + PTs, and VIs + TFs + PTs). Four regression algorithms were adopted: RF, AdaBoost, GBRT, and LASSO. RF leverages bagging to aggregate predictions from multiple decision trees, thereby reducing variance and improving robustness. AdaBoost implements boosting by iteratively reweighting samples to minimize bias, whereas GBRT refines this approach through gradient-based optimization of the loss function, enabling the modeling of complex non-linear relationships. LASSO imposes L1 regularization to induce sparsity, facilitating feature selection and reducing model complexity in high-dimensional settings (Wang et al., 2024b). To ensure the generalizability of the conclusions is not compromised by variations in data splits, this study employed robust 6-fold cross-validation (with 15 samples per fold). Sample allocation for each fold adhered to an equal-width binning principle, thereby thoroughly accounting for the distribution of disease severity. Additionally, the coefficient of determination (R^2), root mean square error (RMSE), and mean absolute error (MAE) (Eqs. (5)–(7)) were used to evaluate model performance, with grid search utilized to systematically explore the hyperparameter space.

$$R^2 = 1 - \frac{\sum_{i=1}^{n}(y_i - \widehat{y}_i)^2}{\sum_{i=1}^{n}(y_i - \overline{y})^2} \tag{5}$$

$$\mathrm{RMSE} = \sqrt{\frac{1}{n}\sum_{i=1}^{n}(y_i - \widehat{y}_i)^2} \tag{6}$$

$$MAE = \frac{1}{n}\sum_{i=1}^{n}|y_i - \widehat{y}_i| \tag{7}$$

In the equations, y represents the DI value, y_i is the actual value, $\widehat{y}_i$ is the estimated value, $\overline{y}$ is the mean of the actual values, and n is 15, representing the number of samples in each fold.

3. Results and analysis

3.1. In-situ observations of PTs revealing disease stress levels

Fig. 3 illustrates the numerical differences and response patterns of LCC_{mea}、NBI、LAI_{mea}, and T_c as DI increases. The results indicate that LCC_{mea}, NBI, and LAI_{mea} significantly decreased ($p\text{-}value < 0.001$) in heavily infected samples, with R^2 values of 0.494, 0.364, and 0.249, respectively, when correlated with DI. In contrast, the canopy temperature (T_c) was notably higher in heavily infected samples, with a corresponding R^2 of 0.487. Additionally, a consistency comparison was conducted for the leaf chlorophyll content measured by the Dualex Scientific and SPAD-502. As shown in Fig. S1, a robust linear relationship was observed in the measurements from both instruments ($R^2 = 0.601$). It can be attributed to the predetermined selection of field observation samples and the similar measurement principles of the two chlorophyll meters, both of which rely on the differential transmittance of two infrared or near-infrared light beams. Compared to biochemical parameters such as LCC_{mea} and NBI, the correlation between structural parameter LAI_{mea} and DI is weaker. This is because LAI_{mea} quantifies the overall growth status of vegetation leaves, and its response to disease tends to be delayed. Only when the disease progresses further, causing substantial leaf damage or shedding, does LAI show a significant decrease.

3.2. Sensitivity feature optimization for comprehensive correlation and multicollinearity

3.2.1. VIs set

The single-band images corresponding to the 48 vegetation indices were computed based on the formulas provided in Table S1. For each ESU, a region of interest (ROI) approximately 60 cm × 60 cm in size was extracted around its geographical coordinates, and the average value of all pixels within this area was calculated to construct the candidate feature set for the VIs. Pearson correlation analysis was conducted between different categories of VIs and DI, yielding the statistic R, which measures the strength of their linear relationship, as shown in Table S2. A threshold of $R = 0.40$ was applied, and all VIs, except for mNDI, DATT, MDATT, CTRI1, MCARI, PRI, $CRI_{515,700}$, $PNIR\times CRI_{770}$, and NPQI, were retained after screening. A recursive method was subsequently employed to iteratively eliminate redundant features with a VIF greater than 10 from the candidate feature set, until six vegetation indices, namely Macc01, TCARI, CRI_{550}, PRI_{m1}, WI, and HI_2014, were retained, thereby forming the final VIs set. Multicollinearity diagnostics were performed on all features of the VIs, and the statistical information is recorded in Table S3. In this study, the 90 samples were categorized into three groups based on the DI: mild infection ($0 < DI \le 30\,\%$), moderate infection ($30\,\% < DI \le 50\,\%$), and severe infection ($50\,\% < DI \le 100\,\%$),

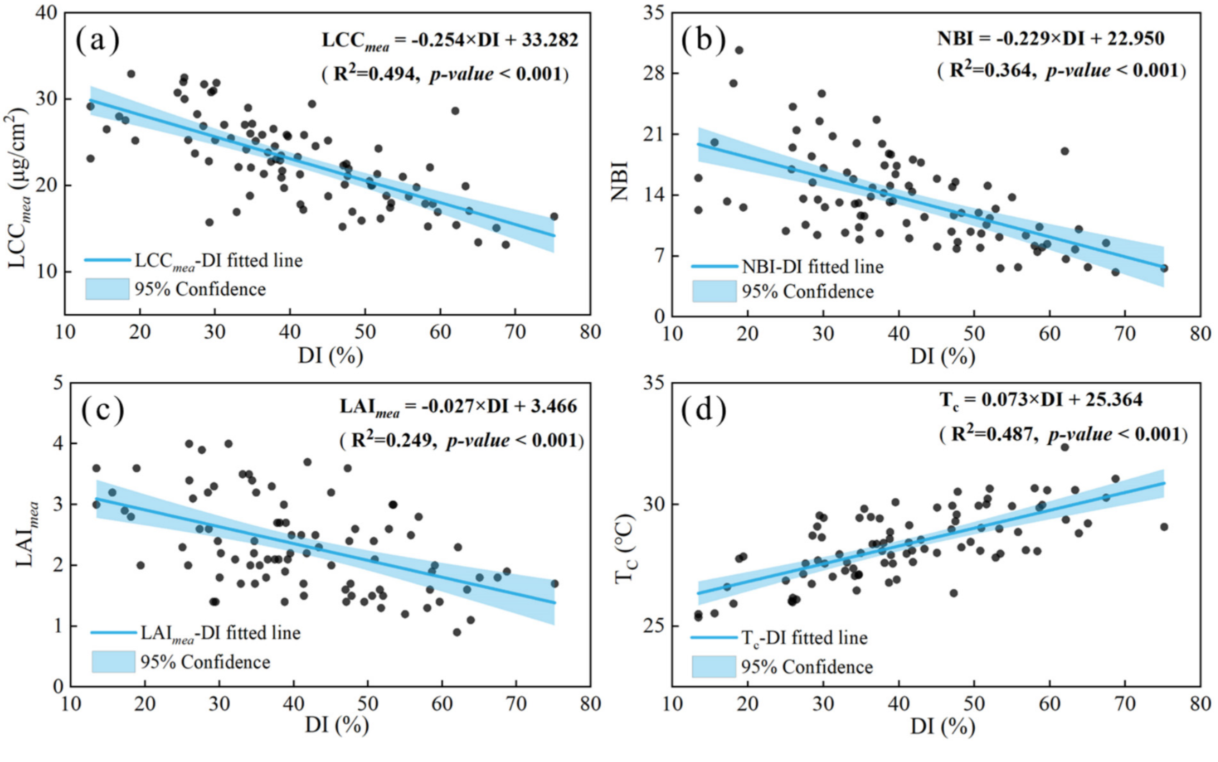

Fig. 3. Response relationship between measured PTs and stripe rust severity levels.

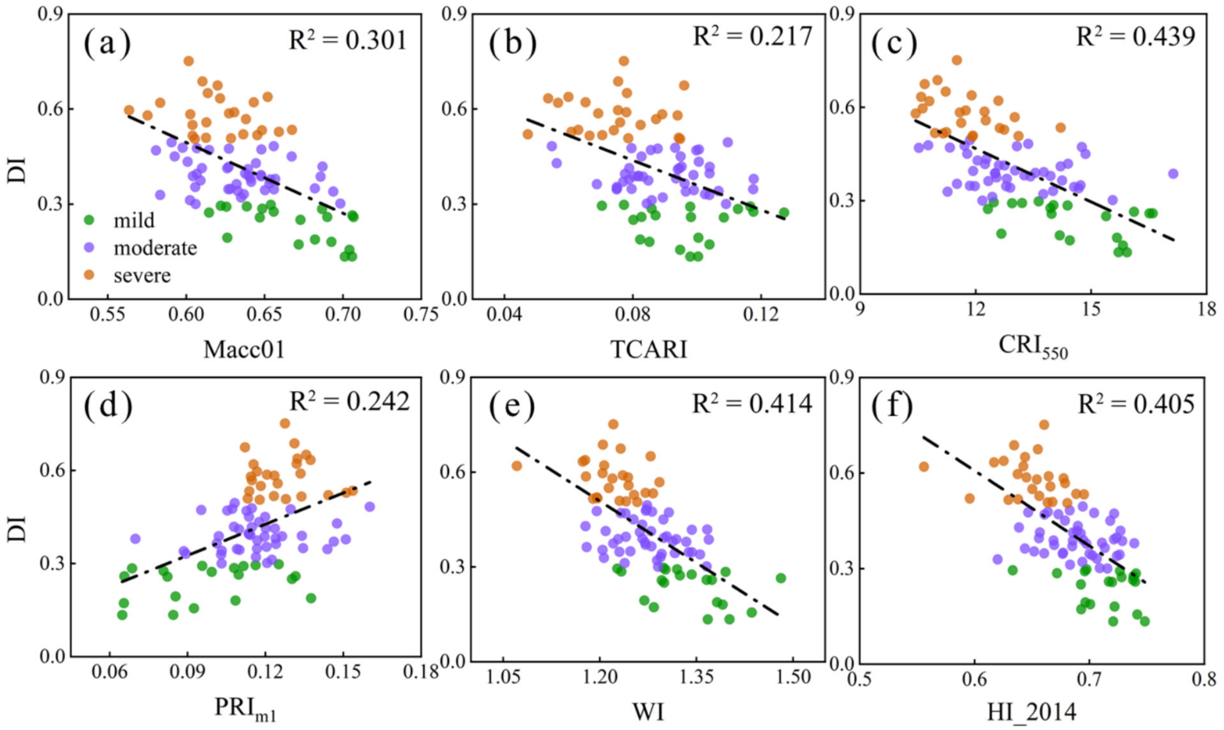

Fig. 4. Linear relationship between samples at different disease severity levels and six VIs.

with sample sizes of 20, 45, and 25, respectively. As shown in Table S3 and Fig. 4, the correlation coefficients of the selected vegetation indices with DI were −0.549, −0.466, −0.662, 0.492, −0.643, and −0.637, while their corresponding VIF values were 6.753, 7.389, 6.667, 2.899, 6.395, and 9.711, with all tolerances exceeding 0.1. Although the final selected VIs were not always the most strongly correlated with DI (for example, the absolute correlation coefficient of NDVI reached 0.728 but was not retained), the two-step filtering approach ensured a balance between correlation and multicollinearity among the features, thereby enhancing the stability of the model.

3.2.2. TFs set

Multi-class TFs were extracted from the three principal component maps using different window sizes, and their relationships with the DI were subsequently analyzed. As illustrated in Fig. 5, Var1, Cor1, Cor2, and Cor3 did not satisfy the correlation threshold (i.e., $R \geq 0.40$) across the entire range of sliding window sizes. Moreover, a total of 11 TFs (more than half of the remaining features) exhibited progressively enhanced associations with DI as the window size increased. Their absolute R exhibited a monotonically increasing trend, peaking at a window size of 17 × 17. These features are Mea1, Hom1, Con1, Dis1, Mea2, Hom2, Dis2, Mea3, Hom3, Con3, and Dis3. Thus, a 17 × 17 window size was considered optimal for accurately matching the spatial aggregation pattern of disease, effectively balancing local details with global information. Further VIF analysis retained 9 TFs: Mea1, Sem1, Mea2, Var2, Con2, Sem2, Mea3, Var3, and Con3. Detailed statistical information, including Variance Proportions and Tolerance, can be found in Table S4. As indicated by Table S4 and Fig. 6, the correlation coefficients between these TFs and DI were 0.615, 0.406, 0.713, −0.463, −0.560, 0.585, 0.425, −0.431, and −0.577, with corresponding VIF values of 6.113, 3.715, 4.174, 4.699, 7.010, 7.883, 2.910, 4.870, and 4.751. Compared to VIs, the final number of retained TFs was higher. This is because PCA, through orthogonal transformation, maps the original features to the principal component space, removing much of the redundant information by retaining maximum variance, resulting in fewer features filtered out by VIF. In contrast, the high correlation of original bands led to stronger multicollinearity among vegetation indices.

3.3. Inversion of PTs from hyperspectral images based on HIMs

When incorporating AL for empirical trait parameter inversion, in order to reduce the impact of sample representativeness on the overall model performance, this study tested five different lookup table sizes (1000, 1500, 2000, 2500, and 3000 samples). The R^2 and RMSE between the measured and estimated values of LCC, LAI, and CCC are presented in Table S5. Specifically, the optimal HIM for empirical trait parameters was not directly determined by the number of samples in the lookup table. For instance, when the lookup table sizes were 2000, 1500, and 2500, the inversion models for LCC, LAI, and CCC achieved the best performance (Fig. 7), with R^2 values of 0.350, 0.577, and 0.596, and RMSE values of 3.943, 0.486, and 0.160, respectively. However, when the lookup table sizes were 3000, 1000, and 3000, the corresponding inversion models performed the worst, with R^2 values of only 0.117, 0.538, and 0.509, and RMSE values of 5.139, 0.510, and 0.187. These results indicate that the quality (representativeness) of the training dataset is crucial for achieving the optimal HIM using GPR, rather than the quantity of samples. As shown in Fig. 7, CCC, which incorporates canopy structural information, significantly outperformed LCC in terms of inversion accuracy. This improvement is attributed to the fact that both the directional reflectance output from the PROSAIL model and airborne hyperspectral reflectance measurements capture the light absorption characteristics of total canopy chlorophyll. These signals are influenced not only by the leaf-level optical properties governed by LCC but also by canopy structural factors such as LAI, leaf angle distribution, and canopy height. Therefore, the CCC derived from the HIM is more effective in revealing the overall impact of wheat stripe rust at the canopy scale.

In addition, this study employed a LUT with 10,000 simulated spectra to invert three non-observed PTs, namely Car, Anth, and CBC, using the GPR algorithm. Fig. 8 illustrates the response patterns of inverted PTs and measured T_c through boxplots, clearly depicting how they

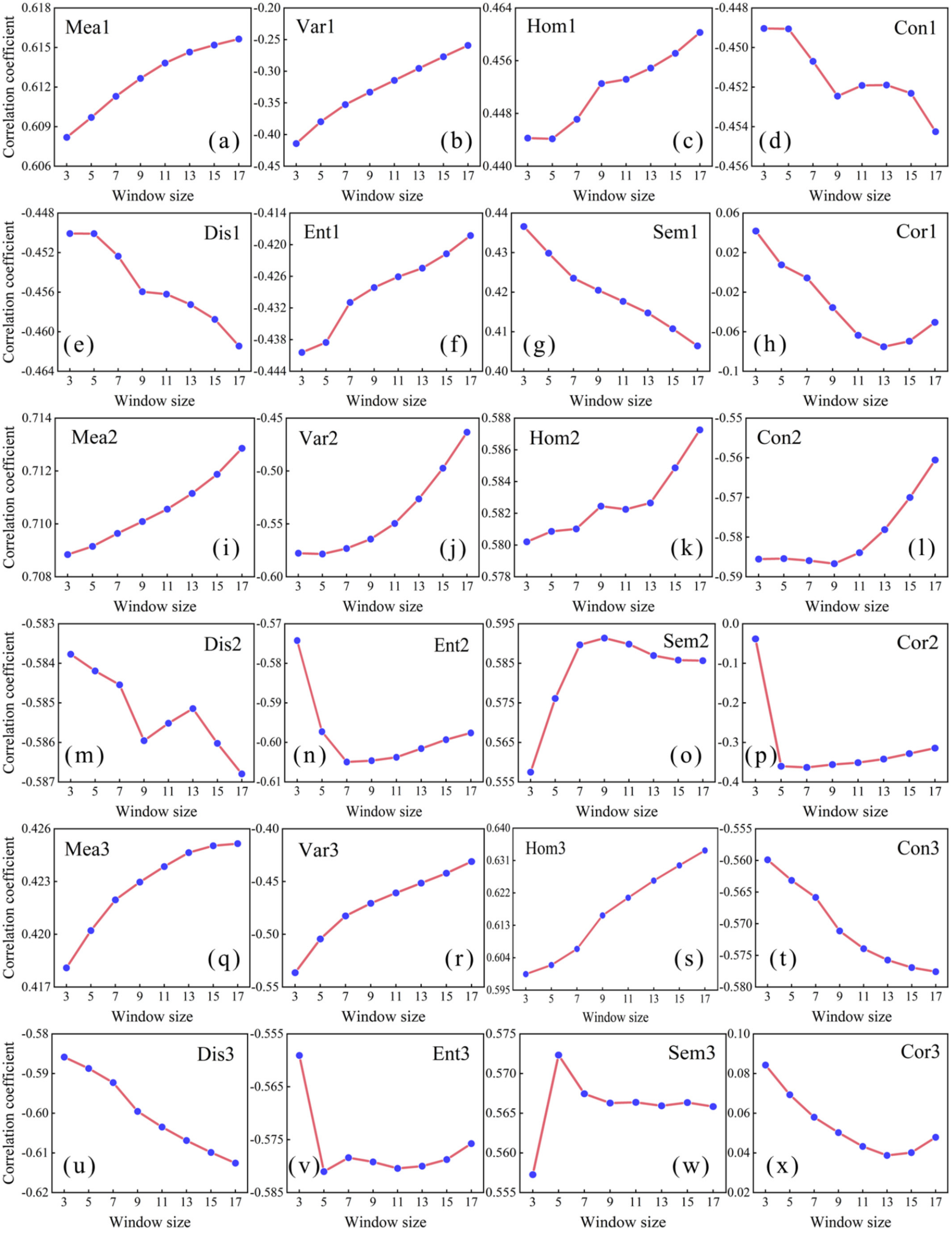

Fig. 5. Relationship between multi-type TFs at different window sizes and DI. PC1: (a)–(h), PC2: (i)–(p), PC3: (q)–(x).

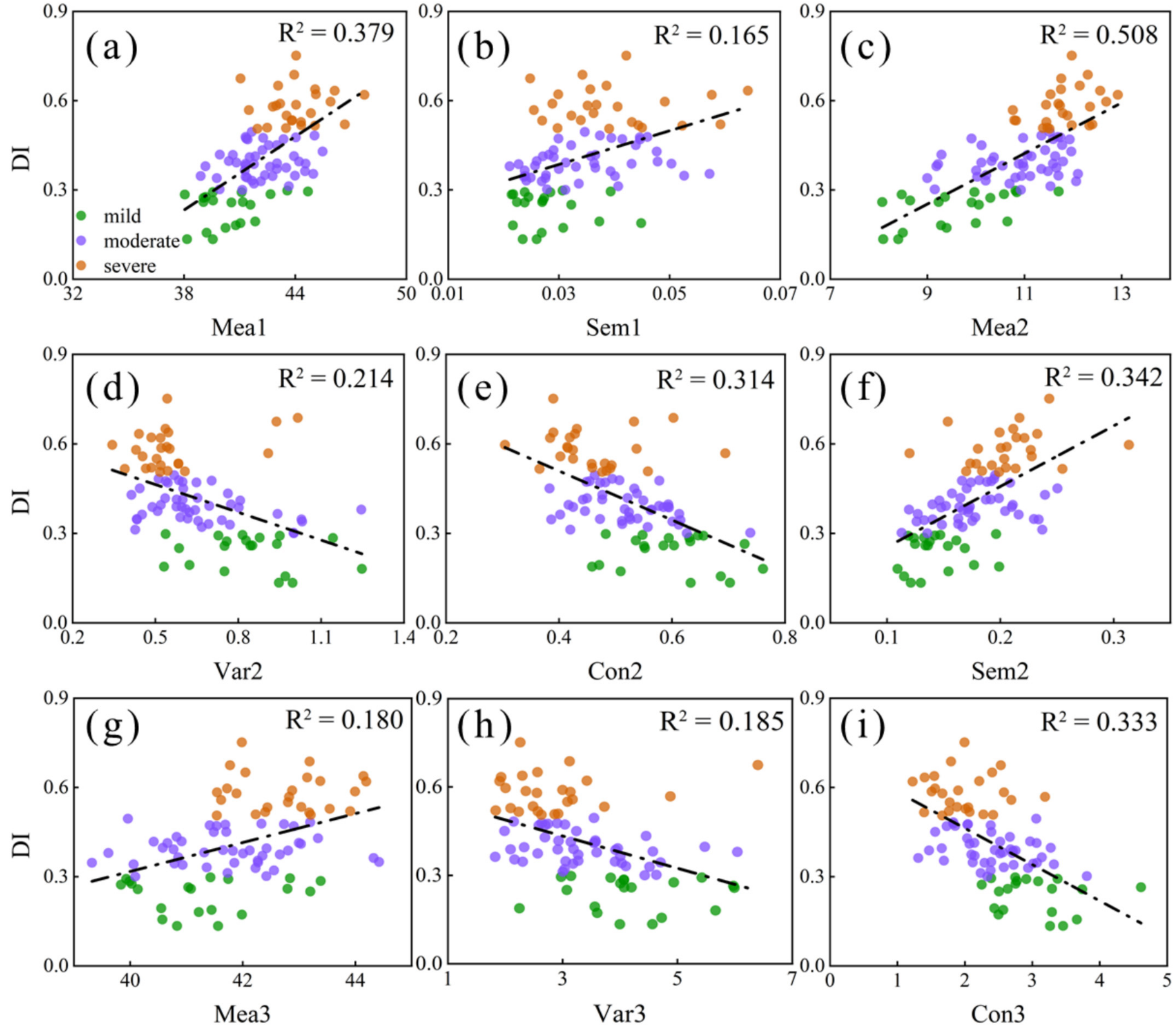

Fig. 6. Linear relationship between samples at different disease severity levels and nine TFs.

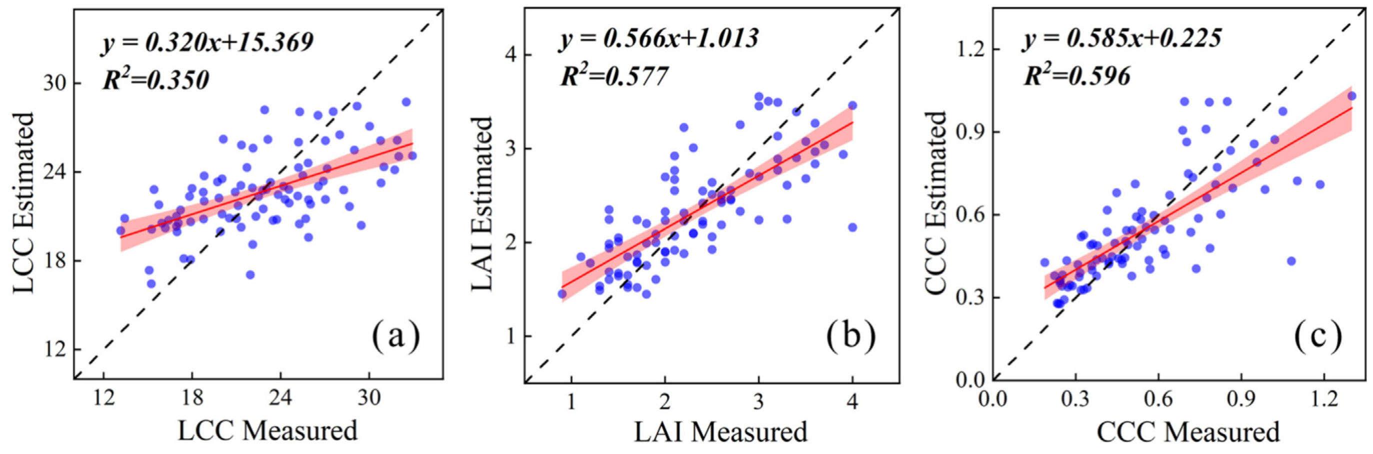

Fig. 7. Relationship between measured and estimated values of LCC, LAI, and CCC (the optimal HIM with AL integration).

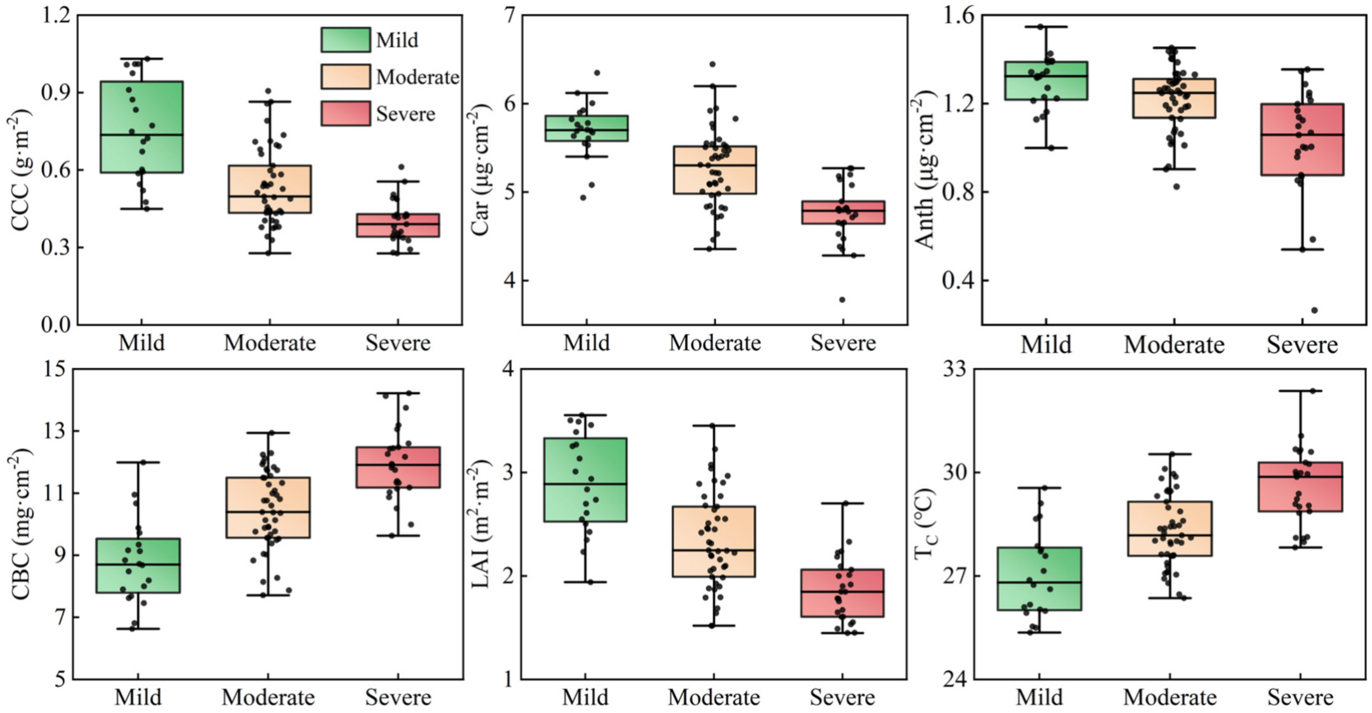

Fig. 8. Relationship between PTs retrieved from hyperspectral and thermal imagery and disease severity.

vary with the increasing severity of stripe rust. The results indicate that all PTs exhibit strict regularity, primarily characterized by a decrease in pigment content (CCC, Car, and Anth) and LAI, while CBC and T_c increase. For example, the average values of CCC, Car, LAI, and T_c are 0.752, 5.694, 2.893, and 27.046 for mildly infected samples; 0.533, 5.271, 2.340, and 28.296 for moderately infected samples; and 0.402, 4.755, 1.866, and 29.592 for severely infected samples. It was found that T_c demonstrates a strongly significant negative correlation with LAI, yielding a coefficient of determination (R^2) of 0.669 (Fig. S2). This results from the progressive development of the disease, which induces leaf chlorosis, wilting, and shedding. Consequently, changes in vegetation biomass and structure reduce the canopy's ability to shade and regulate evapotranspiration, allowing more heat from the soil and vegetation surface to be reflected and accumulated, thus driving a rise in temperature.

3.4. Multi-feature collaborative wheat stripe rust monitoring model construction

This study employed VIF to select VIs and TFs, ensuring minimal redundancy among the variables within the feature set. However, the simple concatenation of features in combination methods imposes higher requirements on the interaction effects between the feature sets. Based on Kendall's tau coefficient, correlation analysis was performed for three types of feature sets, with the results visualized in a heatmap (Fig. 9). Red and blue represent positive and negative correlations, respectively, with circle size reflecting the absolute correlation coefficient. An "×" indicates no significant correlation (*p-value* < 0.001). Kendall's tau is a pairwise, non-parametric method that does not depend on the specific distribution or values of the data, but rather emphasizes the relative ordering of the variables. It is particularly suited for non-linear or non-normally distributed data. The correlation coefficients (τ) were computed for all pairwise combinations of 21 variables, yielding 210 distinct pairs. A threshold of $|\tau| \geq 0.8$ was established to identify redundant feature pairs, and only 7 combinations exceeded the specified threshold, indicating that the feature set is mainly complementary. Given that multi-feature collaborative modeling focuses more on the joint effects of all variables, the average $|\tau|$ between each feature and the remaining 20 features was further calculated, with the relevant information provided in Table S6. The average $|\tau|$ for all features ranged from 0.319 (for PRI_{m1}) to 0.589 (for Mea2), indicating a low level of inter-redundancy, and thus, no variables need to be excluded.

Single feature sets (VIs, TFs, and PTs), as well as their combinations (VIs + TFs, VIs + PTs, TFs + PTs, and VIs + TFs + PTs), were input into four machine learning algorithms: RF, AdaBoost, GBRT, and LASSO, to develop 28 distinct wheat stripe rust disease monitoring models. Performance was evaluated using 6-fold cross-validation, and the results are presented in Table 4. For single features, regardless of the modeling approach, PTs showed the highest accuracy, outperforming VIs and TFs consistently. For instance, when applying the LASSO algorithm, the PTs data source yielded R^2, RMSE, and MAE values of 0.593, 8.53 %, and 7.13 %, respectively. In comparison, the VIs data source showed values of 0.541, 9.00 %, and 7.66 %, while the TFs data source exhibited values of 0.529, 9.22 %, and 7.89 %, respectively. Among the best-performing models built with each algorithm's optimal feature combination, the performance order was: LASSO > AdaBoost > GBRT > RF. For combined features, the modeling results from both the LASSO and AdaBoost algorithms demonstrated that any combination of two or three data sources enhanced the accuracy of wheat rust disease monitoring. For example, when applying the AdaBoost algorithm, the R^2, RMSE, and MAE for the PTs data source were 0.576, 8.65 %, and 6.93 %, respectively; for the TFs data source, these values were 0.465, 9.62 %, and 7.78 %; and for the PTs + TFs combination, they were 0.605, 8.14 %, and 6.76 %. In conclusion, the optimal model was obtained by combining all three feature types for LASSO regression (Fig. 10), achieving R^2, RMSE, and MAE values of 0.628, 8.03 %, and 6.57 %, respectively. This resulted in accuracy improvements of 5.90 %, 18.71 %, 16.08 %, 2.11 %, 4.49 %, and 8.09 % compared to models using PTs, TFs, VIs, PTs + TFs, PTs + VIs, and TFs + VIs as data sources.

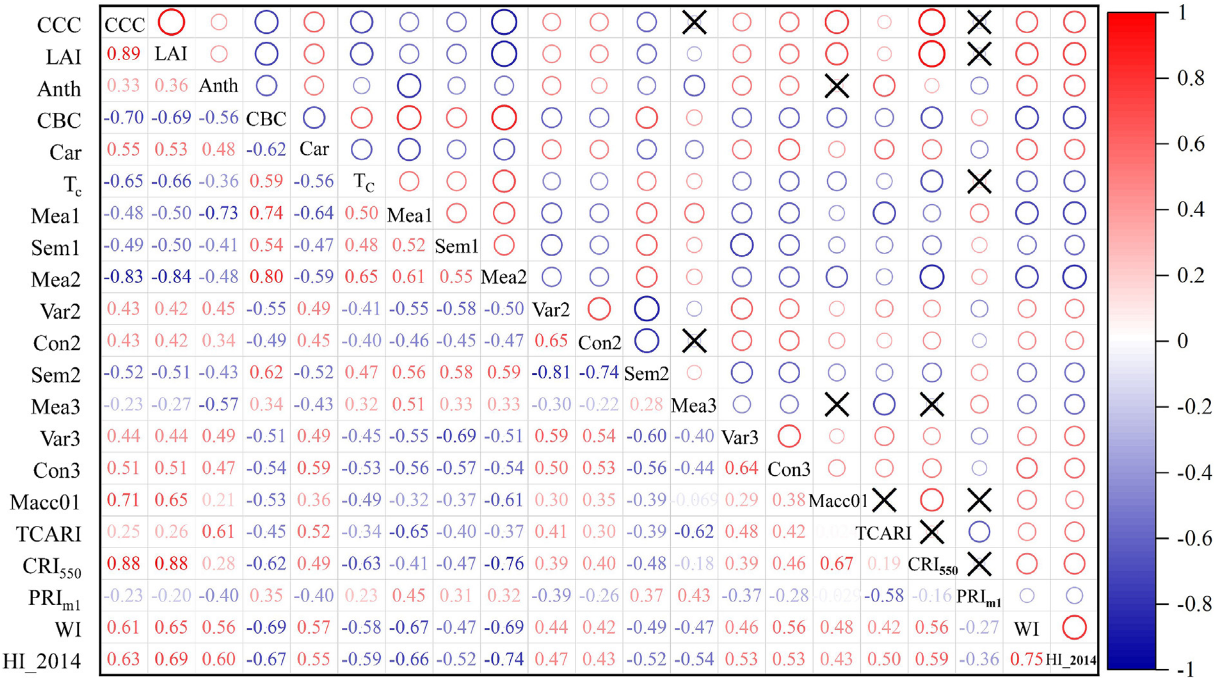

Fig. 9. Comprehensive evaluation of redundancy in VIs, TFs, and PTs based on Kendall's tau coefficient.

4. Discussion

4.1. Sensitivity of VIs, TFs, and PTs to plant-pathogen interactions

Before extracting VIs, TFs, and PTs from UAV hyperspectral data, this study initially analyzed in-situ measurements of LCC_{mea}, NBI, LAI_{mea}, and T_c. With the progression of stripe rust, LCC_{mea}, NBI, and LAI_{mea} consistently decreased, while T_c exhibited a significant increase. These observations are in strong accordance with the findings of Shi et al. (2018) and Hornero et al. (2024). These alterations are intricately linked to the pathogen's disruption of the host's physiological functions. The wheat stripe rust fungus restricts chlorophyll synthesis by infecting the leaves, and the concomitant damage to plant organs further impairs the wheat's ability to absorb and transport nitrogen, leading to a decline in nitrogen status, which is directly reflected in the reduction of NBI (Raya-Sereno et al., 2024). As the intensity and duration of the stress escalate, the affected PTs shift from biochemical to structural characteristics, with the vegetation displaying marked phenotypic variations (Berger et al., 2022). For example, prolonged damage causes extensive leaf death and shedding, resulting in a decrease in LAI_{mea} as a stress indicator. The differences in heat conduction arising from abnormal respiration and transpiration rates under stress further strengthen the correlation between DI and canopy temperature (Zarco-Tejada et al., 2021). Specifically, increased disease severity often leads to stomatal closure and impaired xylem water transport, resulting in reduced transpiration and diminished evaporative cooling capacity, which in turn causes a measurable rise in canopy temperature.

This study also incorporated HIMs integrated with AL to invert empirical trait parameters, demonstrating that this approach effectively retrieves high-confidence PTs from hyperspectral data. The essence of AL is to strategically select the most informative samples from an unlabeled pool, using strategies such as uncertainty, representativeness, or diversity, so as to achieve the highest possible model performance with minimal data. As shown in Fig. 11, progressively adding samples to the initial pool leads to a consistent improvement in the inversion model's performance, which reaches its optimum after all samples in the LUT have been explored. For example, the inversion models for LCC, LAI, and CCC achieved their best performance with 54, 91, and 253 samples in the pool, yielding R^2 values of 0.350, 0.577, and 0.596, and RMSE values of 3.943, 0.486, and 0.159, respectively. The results further indicated that CCC, which incorporates canopy structure information, is more suitable for disease monitoring, as its reduction reflects two coupled effects of stripe rust infection: decreased leaf chlorophyll concentration due to chloroplast damage and pigment degradation, and diminished leaf area caused by wilting and defoliation of infected leaves. Additionally, considering the spectral limitations of UAV hyperspectral

Table 4
Model evaluation based on 6-fold cross-validation.

Algorithm	Input features	Evaluation indexes		
		R^2	RMSE (%)	MAE (%)
RF	PTs	0.559	8.77	7.27
	TFs	0.443	9.88	7.78
	VIs	0.534	9.13	7.68
	PTs + TFs	0.579	8.68	7.02
	PTs + VIs	0.591	8.53	7.04
	TFs + VIs	0.516	9.20	7.70
	PTs + TFs + VIs	0.568	8.71	7.42
AdaBoost	PTs	0.576	8.65	6.93
	TFs	0.465	9.62	7.78
	VIs	0.483	9.65	8.14
	PTs + TFs	0.605	8.14	6.76
	PTs + VIs	0.588	8.51	6.87
	TFs + VIs	0.496	9.52	8.06
	PTs + TFs + VIs	0.583	8.57	6.99
GBRT	PTs	0.586	8.63	7.05
	TFs	0.490	9.41	7.52
	VIs	0.523	9.16	7.71
	PTs + TFs	0.593	8.51	6.77
	PTs + VIs	0.577	8.68	7.41
	TFs + VIs	0.534	9.05	7.51
	PTs + TFs + VIs	0.573	8.64	7.22
LASSO	PTs	0.593	8.53	7.13
	TFs	0.529	9.22	7.89
	VIs	0.541	9.00	7.66
	PTs + TFs	0.615	8.28	6.68
	PTs + VIs	0.601	8.29	6.76
	TFs + VIs	0.581	8.50	7.34
	PTs + TFs + VIs	0.628	8.03	6.57

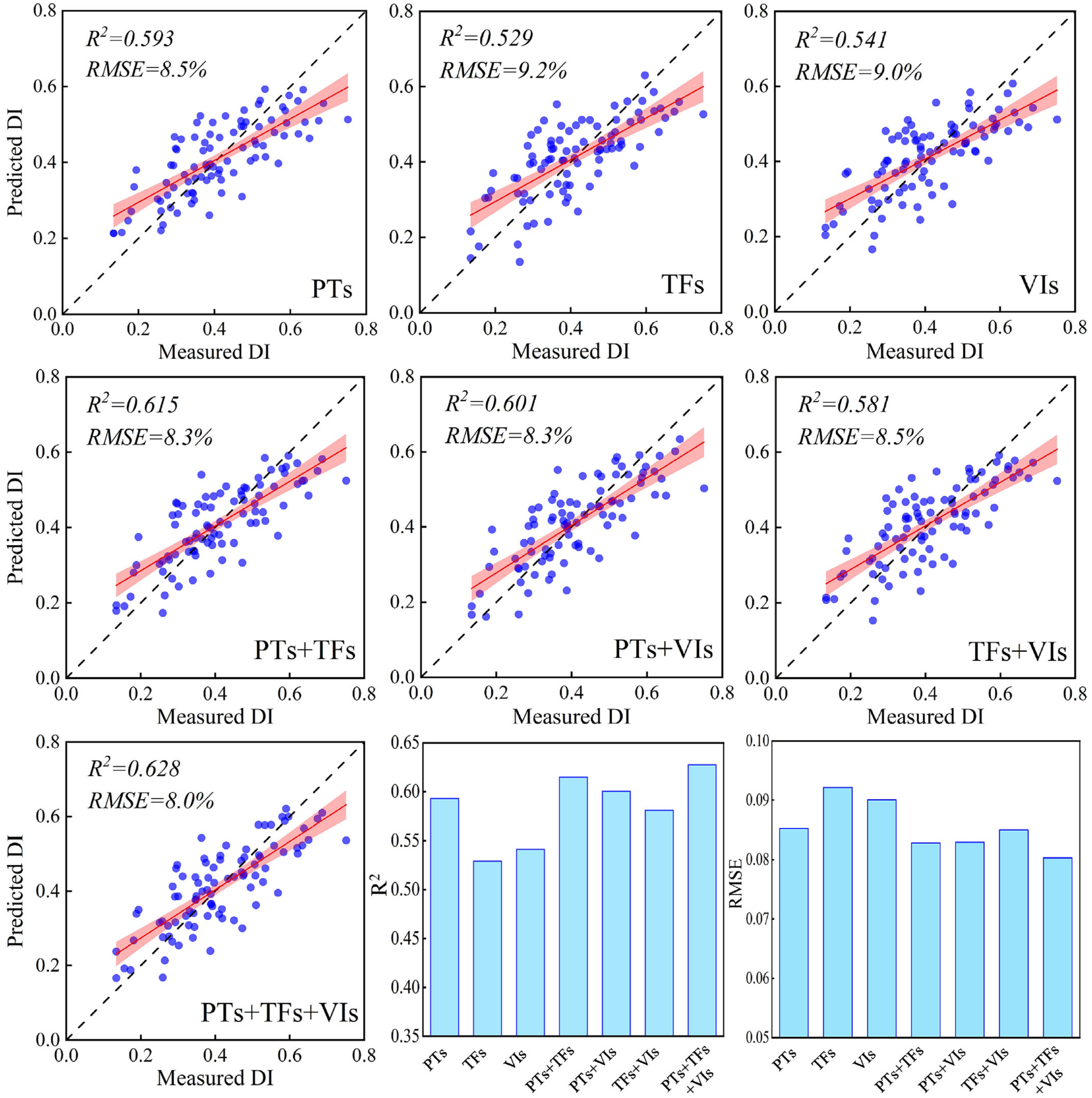

Fig. 10. Comparison of measured and estimated DI values (using the LASSO algorithm with different variable combinations).

sensors, GPR was applied to invert three non-observed PTs: Car, Anth, and CBC. The boxplots for different disease severity levels (Fig. 8) indicate that the inverted non-observed PTs demonstrate high reliability, both in terms of their value distribution range and their trend with disease progression. As stripe rust advances from mild to severe, the pigment contents of Car and Anth progressively decrease, while CBC exhibits an upward trend. This observation is well-supported by previous studies (Hornero et al., 2024; Hornero et al., 2021). The increase in CBC is associated with functional loss and the accumulation of senescent material. Specifically, infected tissues exhibit reduced α-amylase activity, which hampers the transfer of photosynthetic products and results in starch accumulation. Furthermore, the increased input of photosynthetic products from healthy tissues may exacerbate this phenomenon.

A two-step filtering method identified six VIs, including Macc01, TCARI, CRI_{550}, PRI_{m1}, WI, and HI_2014. These indices, which are linked to pigments, water content, and stress conditions, prove to be effective indicators for disease monitoring. The correlation coefficients between these indices and the DI were −0.549, −0.466, −0.662, 0.492, −0.643, and −0.637, respectively. For example, Li et al. (2019) demonstrated that regression models for leaf chlorophyll content were developed using the Macc01 derived from both directional-hemispherical reflectance factor (DHRF) and bidirectional reflectance factor (BRF) spectra, with R^2 values reaching 0.92 and 0.89, respectively. Notably, in this study, the PRI_{m1} values increased as the disease progressed. Guo et al. (2024a) also found similar trends for PRI_{m2} and PRI_{m3}. As an extension of PRI, PRI_{m1} is a sensitive spectral index for lutein cycling,

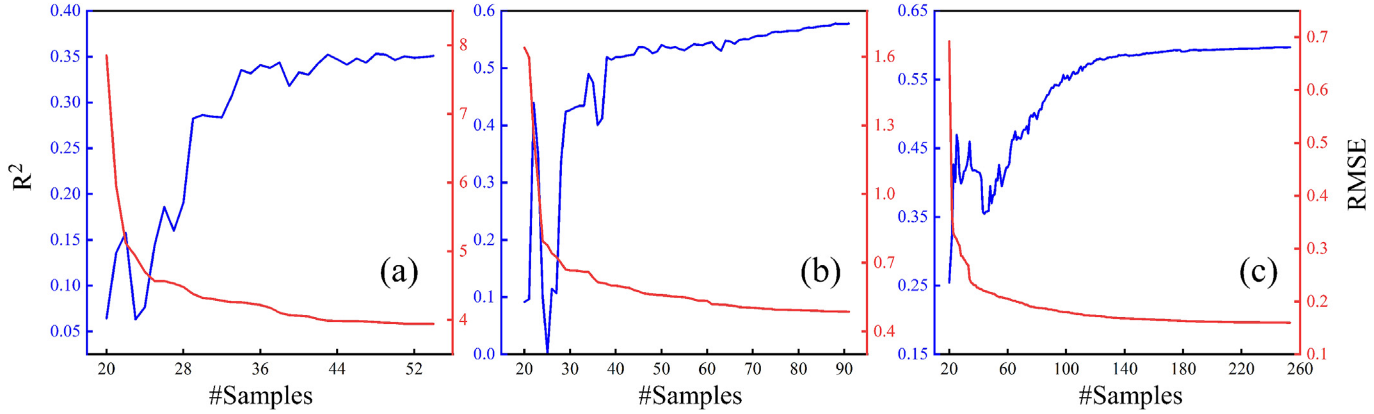

Fig. 11. Goodness-of-fit results (R^2 and RMSE) of AL-based inversion for empirical parameters: (a) LCC, (b) LAI, and (c) CCC.

which can capture plant photosynthetic performance under external stress conditions and is generally negatively correlated with light energy use efficiency (Hikosaka and Noda, 2019; Nakamura et al., 2024). Continuous disease infection reduces the crop's light energy use efficiency, leading to an increase in PRI_{m1}. Furthermore, the fissures generated during rust spore formation, along with the impairment of stomatal function, result in a marked reduction in the water content of infected leaves, which makes WI a valuable metric for monitoring disease severity. Several indices, including NPQI, CTRI1, and DATT, exhibited limited associations with DI, likely due to their weak responsiveness to early physiological disruption or subtle canopy structural changes. Additionally, signal saturation under severe infection may constrain their dynamic sensitivity, underscoring the importance of selecting physiologically relevant and temporally stable indicators for disease assessment.

In the study area (Fig. 1b), the wheat planting density and orientation were uniform throughout the field. As a result, the window size emerged as a crucial factor in determining the effectiveness of TFs. Selecting an optimal window for texture calculation enables a more accurate depiction of the disease's spatial distribution, thereby improving the precision of the models (Xiao et al., 2021). As shown in Fig. 5, a window size of 17 × 17 was optimal for striking a balance between local details and global information. This aligns with the actual conditions of the field, where the overall wheat disease severity is relatively high. This result also avoids issues associated with small window sizes, where disease information may be retained, but similar textures could be misclassified. Ultimately, nine TFs, including Mea1, Sem1, Mea2, Var2, Con2, Sem2, Mea3, Var3, and Con3, were preserved. The diagnostic utility of these 9 texture features likely stems from their ability to capture spatial heterogeneity in canopy structure caused by non-uniform tissue degradation induced by disease infection. In conclusion, the distinct responses of VIs, TFs, and PTs across samples with varying disease severities provide the foundation for multi-feature collaborative monitoring of wheat rust using UAV hyperspectral data.

4.2. Synergistic effects of multi-source remote sensing data in stripe rust monitoring

With the ongoing advancements in sensor payloads and signal processing technologies, the variety and volume of data obtainable through remote sensing methods have been steadily expanding. Multi-dimensional information regarding morphology, structure, biochemistry, pathology, and the environment is expected to be extracted from crop canopy spectra (Song et al., 2025). Different crop indices have distinct characteristics, and their complementary advantages can enhance the accuracy and efficiency of disease monitoring. VIs primarily capture pigment-related spectral variations, TFs emphasize structural heterogeneity, and PTs reflect physiological status. Their integration forms a physiological-spectral–morphological synergy that enhances model robustness. The sensitivity of VIs, TFs, and PTs to plant-pathogen interactions has deepened scholars' comprehensive understanding of disease dynamics, enabling more targeted improvements in disease monitoring strategies. Furthermore, the application of machine learning algorithms for modeling based on disease information extraction is increasingly essential. Compared to traditional statistical models, these algorithms are better equipped to handle high-dimensional data that include noise and non-linear relationships, thereby creating disease monitoring models with stronger generalization ability and robustness. Therefore, this study utilized four algorithms, namely RF, AdaBoost, GBRT, and LASSO, to develop 28 wheat rust disease monitoring models based on both feature subsets and all feature combinations.

For single-source feature sets, PTs consistently exhibited superior performance over VIs and TFs, a trend that proved robust across all tested algorithms. The observed variation was limited to the magnitude of algorithmic performance, which followed the order: LASSO > GBRT > AdaBoost > RF. This finding suggests that PTs are more advantageous in indicating vegetation performance, stress, and allocation, and are intimately connected to plant health and responses to biotic stress (Watt et al., 2023). For example, the decrease in pigments such as CCC and Car uncovers the chlorophyll degradation processes triggered by changes in photoprotective mechanisms due to disease infection; the increase in T_c illustrates the deterioration of canopy structure and abnormal transpiration. VIs and TFs performed relatively poorly, mainly because they provide indirect insights into plant conditions and are susceptible to external environmental factors. For instance, TFs can partially capture canopy structural variations induced by pathogen attacks; however, this variation is strongly influenced by physiological and biochemical stress responses and is difficult to detect during the early stages of disease (Ma et al., 2024).

For combined features, four algorithms robustly confirmed that integrating multiple data sources substantially outperformed any single-source approach in terms of model accuracy. When all three feature types were combined for LASSO regression, the optimal model achieved R^2, RMSE, and MAE values of 0.628, 8.03 %, and 6.57 %, respectively. This resulted in accuracy improvements of 5.90 %, 18.71 %, 16.08 %, 2.11 %, 4.49 %, and 8.09 % compared to models using PTs, TFs, VIs, PTs + TFs, PTs + VIs, and TFs + VIs as data sources. In this study, the exceptional performance of LASSO stems from its robust feature selection capability. During the regression process, LASSO utilizes L1 regularization, which penalizes the coefficients of less relevant features, driving them toward zero. This mechanism effectively eliminates irrelevant or redundant features, reduces overfitting, and enhances the model's generalization ability (Wang et al., 2024b). On the other hand, ensemble learning algorithms such as RF, AdaBoost, and GBRT rely primarily on multiple decision trees. During training, they may become overly sensitive to noise or redundant features, leading to overfitting and consequently weaker model performance.

To further elucidate the synergistic effects of multi-source data, this study utilized SHapley Additive exPlanations (SHAP) to quantify the positive and negative impacts of multiple variables to the output (DI) in models constructed with the optimal feature-algorithm combinations. SHAP, introduced in 2017, leverages game-theoretic principles to effectively interpret machine learning model outputs and generate feature attributions for individual instances. It has found widespread application in fields such as yield prediction, lodging detection, and disease monitoring (Ahmed et al., 2024; Han et al., 2022; Li et al., 2023). Fig. 12 illustrates the SHAP visualization analysis of the top 15 features from the optimal monitoring model, comprising both a swarm plot and a bar chart. The swarm plot, with widely distributed samples, reveals the specific influence of the current features on DI, with red and blue dots representing positive and negative contributions to the model's output, respectively. In the bar chart, the length of each bar represents feature importance, computed as the mean absolute SHAP value (Adali et al., 2022), with the corresponding values for all features in each subplot summarized in Table S7. As shown in Fig. 12(a), when all samples (mild, moderate, and severe) were included in the modeling, the top 10 features ranked by importance were Mea1, Car, CBC, Sem1, CCC, HI_2014, LAI, $\mathrm{PRI}_{\mathrm{m1}}$, $\mathrm{T_c}$, and Con2. The interleaved ranking of different feature types indicates a synergistic interaction among

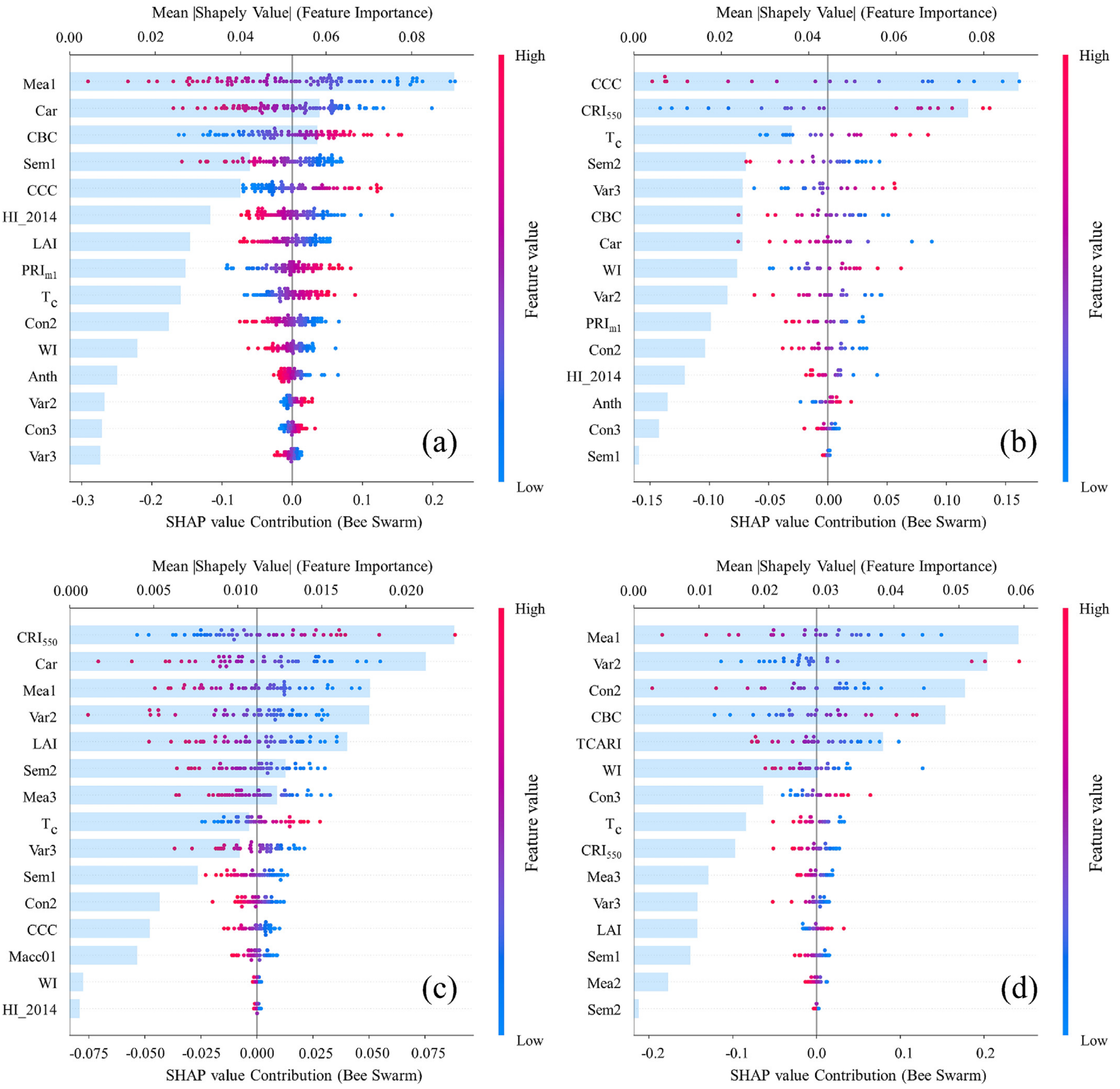

Fig. 12. SHAP-based feature importance for stripe rust monitoring using the optimal LASSO model, displaying the top 15 features ranked by SHAP values: (a) combined dataset (mild, moderate, severe), (b) mild, (c) moderate, and (d) severe infection samples.

features rather than independent contributions. However, such aggregated analysis does not disentangle the dominant roles and complementary interactions of VIs, TFs, and PTs at different stages of disease development.

To address this limitation, stage-specific SHAP analyses were performed for mild, moderate, and severe infections (Figs. 12b–d). The results demonstrate a distinct stage-dependent dominance of feature categories, closely aligned with the pathophysiological trajectory of stripe rust. At the mild stage, PTs emerged as the leading contributors, particularly canopy chlorophyll content (CCC) and canopy temperature (T_c). This dominance reflects the early disruption of chloroplast integrity and pigment synthesis by the pathogen, leading to reduced photosynthetic capacity. Concurrent stomatal closure further limits transpiration, causing a slight elevation in canopy temperature—explaining why PTs, which are directly linked to physiological status, exhibit the highest sensitivity during early infection. At the moderate stage, VIs assumed primary importance, capturing pronounced changes in canopy reflectance as lesions expanded and pigment degradation accelerated. Indices sensitive to red-edge and near-infrared shifts effectively characterize the combined pigment and structural damage, making VIs the most diagnostic indicators at this stage. In the severe stage, TFs displayed a marked increase in contribution, becoming the dominant feature category. This trend is consistent with extensive tissue necrosis and leaf abscission, which dramatically increase canopy spatial heterogeneity and alter image texture, rendering TFs highly responsive to late-stage disease severity.

Collectively, these findings highlight a dynamic complementarity among the three feature types: PTs provide early detection through physiological signals, VIs capture mid-stage spectral–structural alterations, and TFs dominate when morphological disruption becomes severe. This physiological-spectral–morphological synergy not only clarifies the mechanistic underpinnings of disease progression but also reinforces the value of multisource feature integration for comprehensive, full-cycle monitoring of wheat stripe rust.

4.3. Challenges and prospects

This study represents the pioneering effort to integrate inverted PTs, VIs, and TFs for collaborative modeling in wheat stripe rust monitoring, demonstrating that multi-source remote sensing data significantly enhance the accuracy of DI estimation. The PTs retrieved from the measured hyperspectral data using the HIMs include LAI, CCC, Car, Anth, and CBC. However, considering the physiological and structural changes in crops due to pathogen infection, it is evident that other input parameters of the PROSAIL model, such as EWT, C_p, and ALA, also hold potential for indicating stress conditions. The primary limitation in applying these parameters is the spectral mismatch between their sensitive wavelengths and the detection range of the 410 SHARK sensor. For example, the optimal spectral range for estimating C_p is 1500–1700 nm (Féret et al., 2021), and the three primary absorption bands of leaf water are located between 1350 and 2500 nm. Although full-spectrum hyperspectral imaging covering 400–2500 nm provides a potential solution, its application remains challenging in field and airborne conditions due to high costs, atmospheric water vapor absorption, and the sharp decline in signal-to-noise ratio at spectral edges. Moreover, the representativeness of simulated spectral samples generated through the forward RTM directly impacts the performance of inverted PTs. Therefore, it is essential to refine the PROSAIL model by eliminating unrealistic parameter combinations, guided by the measured ranges of empirical parameters (Guo et al., 2024a).

Compared to physiological and biochemical parameters derived from hyperspectral data and canopy temperature obtained from thermal imagery, SIF, which directly reflects vegetation photosynthetic activity, offers superior potential for disease monitoring. Currently, an increasing number of scholars have applied SIF and its derived indices to crop disease research at the near-ground canopy scale (Ren et al., 2023). With the development of hardware-software integration technology, airborne platforms have enabled rapid and reliable SIF measurements at small-scale field levels. Based on this, a limited number of studies have been conducted (Bendig et al., 2019; Wang et al., 2023; Zhang et al., 2022). However, research remains scarce in evaluating the potential of UAV-derived SIF observations for early disease detection or severity monitoring. Moreover, since SIF results from the combined influence of both physiological and structural factors, disentangling non-physiological variations from changes in photosynthetic function would offer a more comprehensive understanding of the canopy's SIF response mechanisms under pathogen infection.

Integration of multisource features has been shown to substantially improve the accuracy of stripe rust monitoring. However, bias analysis (Fig. 13) reveals that under the LASSO model, DI values for severely infected samples are consistently underestimated, whereas mild and moderate cases are overestimated to varying degrees. Specifically,

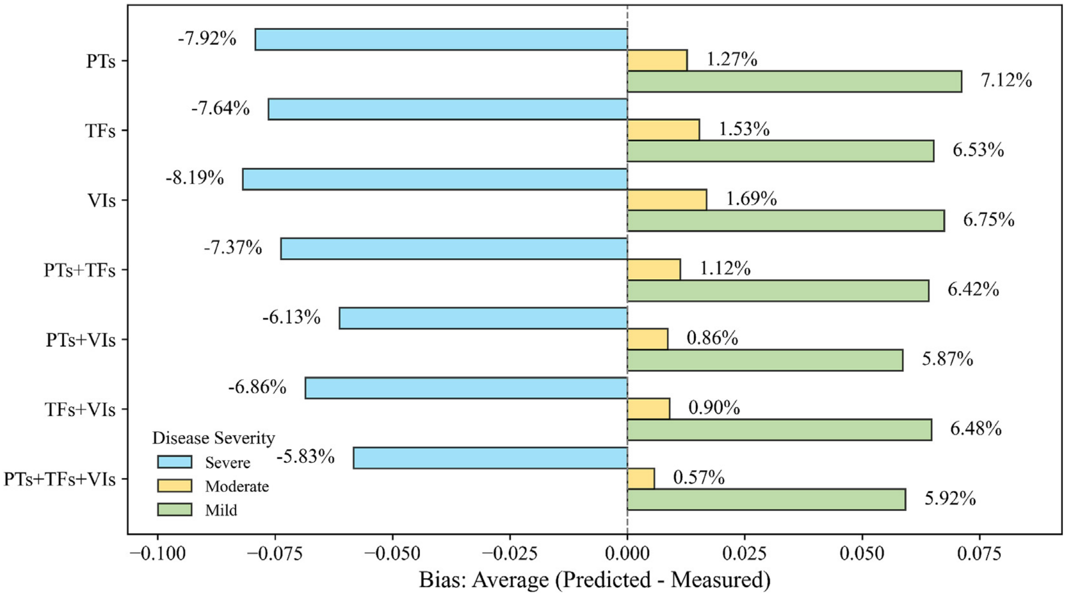

Fig. 13. Prediction bias across disease severity levels under different feature combinations using the LASSO algorithm.

severe cases exhibit biases ranging from −8.19 % to −5.83 %, moderate cases from 0.57 % to 1.69 %, and mild cases from 5.87 % to 7.12 %. This discrepancy partly reflects the pathophysiological progression of stripe rust. At advanced stages, severe chlorosis, tissue necrosis, and a sharp decline in photosynthetic activity cause spectral and structural features to saturate, limiting their ability to distinguish severe infections. From a modeling perspective, LASSO applies a uniform regularization parameter and favors sparse, conservative solutions, which, while mitigating overfitting, constrains its ability to capture complex or nonlinear feature interactions. To address this limitation, two strategies are proposed: (1) Incorporate interaction terms into the linear framework to capture non-additive effects among spectral, structural, and texture features during late infection, while retaining feature selection through L1 regularization to enhance sensitivity to synergistic signals. (2) Introduce biologically informed constraints, such as modeling the monotonic decline of LAI and CCC with increasing severity, implemented via constrained regression or Bayesian regularization, to improve predictive stability under extreme conditions and ensure physiological consistency.

In summary, this study presents a novel and reliable approach for wheat stripe rust monitoring by integrating multi-source features. However, regional variability in climate, soil properties, and wheat varieties may influence the stability and transferability of the proposed models. Future research should incorporate multi-regional datasets to evaluate model generalizability and adaptiveness under diverse agroecological conditions. Given that this study is constrained to single-temporal observations, the dynamic evolution of PTs during early disease onset could not be adequately resolved. Future research also should prioritize multi-temporal remote sensing approaches to capture disease trajectories more comprehensively and to enable earlier and more reliable warning of infection outbreaks. Considering that processing and analyzing multi-source remote sensing data often demands significant human and material resources, which could limit its widespread application in agricultural practices, developing a framework-based data processing pipeline for rapid mapping from UAV imagery would be especially beneficial for efficient and precise crop disease management.

5. Conclusion

This study utilized HIMs to extract PTs from UAV-based hyperspectral imagery and incorporated thermal imagery to obtain T_c, thereby constructing and quantifying the potential of PTs for monitoring wheat stripe rust. Furthermore, PTs were integrated with conventional feature parameters, including VIs and TFs, for the first time in disease monitoring modeling. Experimental results demonstrated that as the severity of wheat stripe rust increased, the inverted PTs and measured T_c exhibited significant responses ($p\text{-value} < 0.001$), primarily reflected in the decline of pigment content (CCC, Car, and Anth) and structural parameter LAI, as well as the increase in CBC and T_c. These findings effectively revealed the biochemical and biophysical variations in infected crops. Using machine learning algorithms (RF, AdaBoost, GBRT, and LASSO), 28 monitoring models were constructed based on both single and combined feature sets. The results indicated that PTs, due to their strong correlation with plant health status and responses to biotic stress, significantly outperformed VIs and TFs. Additionally, the sparse nature of the LASSO algorithm and the synergistic interactions between multiple feature types both contributed to enhanced model accuracy. When the combination of three feature types was applied in LASSO regression to obtain the optimal model, the R^2, RMSE, and MAE values were 0.628, 8.03 %, and 6.57 %, respectively. Compared to models utilizing single data sources (PTs, TFs, VIs) or their combinations (PTs + TFs, PTs + VIs, TFs + VIs), the model's accuracy improved by 5.90 %, 18.71 %, 16.08 %, 2.11 %, 4.49 %, and 8.09 %, respectively. Overall, the integration of PTs, VIs, and TFs in this study enriches the methodological framework for wheat stripe rust monitoring, providing crucial insights for the advancement of large-scale disease detection via airborne and satellite platforms.

CRediT authorship contribution statement

Kehui Ren: Writing – original draft, Validation, Software, Investigation, Data curation. **Anting Guo:** Supervision, Software, Resources, Conceptualization. **Binxiang Qian:** Validation, Methodology, Investigation. **Chao Ruan:** Methodology, Investigation, Data curation. **Wenjiang Huang:** Writing – review & editing, Project administration, Funding acquisition. **Yingying Dong:** Supervision, Resources, Project administration. **Xia Jing:** Investigation, Funding acquisition. **Kun Wang:** Supervision. **Tiecheng Huang:** Formal analysis. **Huiqin Ma:** Methodology.

Declaration of competing interest

The authors declare that they have no known competing financial interests or personal relationships that could have appeared to influence the work reported in this paper.

Acknowledgments

This article was supported by the National Key Research and Development Program of China (2023YFB3906203).

Appendix A. Supplementary data

Supplementary data to this article can be found online at https://doi.org/10.1016/j.aiia.2025.10.006.

References

Adali, T., Kantar, F., Akhonda, M.A.B.S., Strother, S., Calhoun, V.D., Acar, E., 2022. Reproducibility in matrix and tensor decompositions: focus on model match, interpretability, and uniqueness. IEEE Signal Process. Mag. 39, 8–24.

Adeluyi, O., Harris, A., Verrelst, J., Foster, T., Clay, G.D., 2021. Estimating the phenological dynamics of irrigated rice leaf area index using the combination of PROSAIL and Gaussian process regression. Int. J. Appl. Earth Obs. Geoinf. 102, 102454.

Ahmed, T., Wijewardane, N.K., Lu, Y., Jones, D.S., Kudenov, M., Williams, C., Villordon, A., Kamruzzaman, M., 2024. Advancing sweetpotato quality assessment with hyperspectral imaging and explainable artificial intelligence. Comput. Electron. Agric. 220, 108855.

Bendig, J., Malenovský, Z., Gautam, D., Lucieer, A., 2019. Solar-induced chlorophyll fluorescence measured from an unmanned aircraft system: sensor etaloning and platform motion correction. IEEE Trans. Geosci. Remote Sens. 58, 3437–3444.

Berger, K., Rivera Caicedo, J.P., Martino, L., Wocher, M., Hank, T., Verrelst, J., 2021. A survey of active learning for quantifying vegetation traits from terrestrial earth observation data. Remote Sens 13, 287.

Berger, K., Machwitz, M., Kycko, M., Kefauver, S.C., Van Wittenberghe, S., Gerhards, M., Verrelst, J., Atzberger, C., Van der Tol, C., Damm, A., 2022. Multi-sensor spectral synergies for crop stress detection and monitoring in the optical domain: a review. Remote Sens. Environ. 280, 113198.

Camino, C., Calderón, R., Parnell, S., Dierkes, H., Chemin, Y., Román-Écija, M., Montes-Borrego, M., Landa, B.B., Navas-Cortes, J.A., Zarco-Tejada, P.J., 2021. Detection of Xylella fastidiosa in almond orchards by synergic use of an epidemic spread model and remotely sensed plant traits. Remote Sens. Environ. 260, 112420.

Chakhvashvili, E., Siegmann, B., Muller, O., Verrelst, J., Bendig, J., Kraska, T., Rascher, U., 2022. Retrieval of crop variables from proximal multispectral UAV image data using PROSAIL in maize canopy. Remote Sens 14, 1247.

Cotter, M., Asch, F., Hilger, T., Rajaona, A., Schappert, A., Stuerz, S., Yang, X., 2017. Measuring leaf area index in rubber plantations – a challenge. Ecol. Indic. 82, 357–366.

Féret, J.-B., Berger, K., De Boissieu, F., Malenovský, Z., 2021. PROSPECT-PRO for estimating content of nitrogen-containing leaf proteins and other carbon-based constituents. Remote Sens. Environ. 252, 112173.

Gabriel, J.L., Zarco-Tejada, P.J., López-Herrera, P.J., Pérez-Martín, E., Alonso-Ayuso, M., Quemada, M., 2017. Airborne and ground level sensors for monitoring nitrogen status in a maize crop. Biosyst. Eng. 160, 124–133.

Guan, H., Liu, H., Meng, X., Luo, C., Bao, Y., Ma, Y., Yu, Z., Zhang, X., 2020. A quantitative monitoring method for determining maize lodging in different growth stages. Remote Sens 12, 3149.

Guo, A., Huang, W., Qian, B., Wang, K., Liu, H., Ren, K., 2024a. Improved early detection of wheat stripe rust through integration pigments and pigment-related spectral indices quantified from UAV hyperspectral imagery. Int. J. Appl. Earth Obs. Geoinf. 135, 104281.

Guo, A., Huang, W., Qian, B., Ye, H., Jiao, Q., Cheng, X., Ruan, C., 2024b. A hybrid model coupling PROSAIL and continuous wavelet transform based on multi-angle hyperspectral data improves maize chlorophyll retrieval. Int. J. Appl. Earth Obs. Geoinf. 132, 104076.

Han, L., Yang, G., Yang, X., Song, X., Xu, B., Li, Z., Wu, J., Yang, H., Wu, J., 2022. An explainable XGBoost model improved by SMOTE-ENN technique for maize lodging detection based on multi-source unmanned aerial vehicle images. Comput. Electron. Agric. 194, 106804.

Hikosaka, K., Noda, H.M., 2019. Modeling leaf CO2 assimilation and photosystem II photochemistry from chlorophyll fluorescence and the photochemical reflectance index. Plant Cell Environ. 42, 730–739.

Hornero, A., Hernández-Clemente, R., North, P.R., Beck, P., Boscia, D., Navas-Cortes, J.A., Zarco-Tejada, P.J., 2020. Monitoring the incidence of Xylella fastidiosa infection in olive orchards using ground-based evaluations, airborne imaging spectroscopy and Sentinel-2 time series through 3-D radiative transfer modelling. Remote Sens. Environ. 236, 111480.

Hornero, A., Zarco-Tejada, P.J., Quero, J.L., North, P.R., Ruiz-Gómez, F.J., Sánchez-Cuesta, R., Hernández-Clemente, R., 2021. Modelling hyperspectral-and thermal-based plant traits for the early detection of Phytophthora-induced symptoms in oak decline. Remote Sens. Environ. 263, 112570.

Hornero, A., Zarco-Tejada, P., Marengo, I., Faria, N., Hernández-Clemente, R., 2024. Detection of oak decline using radiative transfer modelling and machine learning from multispectral and thermal RPAS imagery. Int. J. Appl. Earth Obs. Geoinf. 127, 103679.

Kwon, S., Shin, J., Seo, I.W., Noh, H., Jung, S.H., You, H., 2022. Measurement of suspended sediment concentration in open channel flows based on hyperspectral imagery from UAVs. Adv. Water Resour. 159, 104076.

Lan, Y., Huang, Z., Deng, X., Zhu, Z., Huang, H., Zheng, Z., Lian, B., Zeng, G., Tong, Z., 2020. Comparison of machine learning methods for citrus greening detection on UAV multispectral images. Comput. Electron. Agric. 171, 105234.

Li, D., Tian, L., Wan, Z., Jia, M., Yao, X., Tian, Y., Zhu, Y., Cao, W., Cheng, T., 2019. Assessment of unified models for estimating leaf chlorophyll content across directional-hemispherical reflectance and bidirectional reflectance spectra. Remote Sens. Environ. 231, 111240.

Li, Y., Zeng, H., Zhang, M., Wu, B., Zhao, Y., Yao, X., Cheng, T., Qin, X., Wu, F., 2023. A county-level soybean yield prediction framework coupled with XGBoost and multidimensional feature engineering. Int. J. Appl. Earth Obs. Geoinf. 118, 103269.

Li, J., Ge, Y., Puntel, L.A., Heeren, D.M., Bai, G., Balboa, G.R., Gamon, J.A., Arkebauer, T.J., Shi, Y., 2024. Integrating UAV hyperspectral data and radiative transfer model simulation to quantitatively estimate maize leaf and canopy nitrogen content. Int. J. Appl. Earth Obs. Geoinf. 129, 103817.

Lijuan, W., Zheng, N., 2014. Sensitivity analysis of vegetation parameters based on PROSAIL model. Remote Sens. Technol. Appl. 29, 219–223.

Liu, Y., Liu, G., Sun, H., An, L., Zhao, R., Liu, M., Tang, W., Li, M., Yan, X., Ma, Y., 2024. Exploring multi-features in UAV based optical and thermal infrared images to estimate disease severity of wheat powdery mildew. Comput. Electron. Agric. 225, 109285.

Ma, R., Zhang, N., Zhang, X., Bai, T., Yuan, X., Bao, H., He, D., Sun, W., He, Y., 2024. Cotton Verticillium wilt monitoring based on UAV multispectral-visible multi-source feature fusion. Comput. Electron. Agric. 217, 108628.

Nakamura, Y., Tsujimoto, K., Ogawa, T., Noda, H.M., Hikosaka, K., 2024. Correction of photochemical reflectance index (PRI) by optical indices to predict non-photochemical quenching (NPQ) across various species. Remote Sens. Environ. 305, 114062.

Pipia, L., Amin, E., Belda, S., Salinero-Delgado, M., Verrelst, J., 2021. Green LAI mapping and cloud gap-filling using Gaussian process regression in Google Earth Engine. Remote Sens 13, 403.

Poblete, T., Navas-Cortes, J.A., Hornero, A., Camino, C., Calderon, R., Hernandez-Clemente, R., Landa, B.B., Zarco-Tejada, P.J., 2023. Detection of symptoms induced by vascular plant pathogens in tree crops using high-resolution satellite data: modelling and assessment with airborne hyperspectral imagery. Remote Sens. Environ. 295, 113698.

Qiu, F., Chen, J.M., Ju, W., Wang, J., Zhang, Q., Fang, M., 2018. Improving the PROSPECT model to consider anisotropic scattering of leaf internal materials and its use for retrieving leaf biomass in fresh leaves. IEEE Trans. Geosci. Remote Sens. 56, 3119–3136.

Raya-Sereno, M.D., Camino, C., Pancorbo, J., Alonso-Ayuso, M., Gabriel, J.L., Beck, P., Quemada, M., 2024. Assessing wheat genotype response under combined nitrogen and water stress scenarios coupling high-resolution optical and thermal sensors with radiative transfer models. Eur. J. Agron. 154, 127102.

Ren, K., Dong, Y., Huang, W., Guo, A., Jing, X., 2023. Monitoring of winter wheat stripe rust by collaborating canopy SIF with wavelet energy coefficients. Comput. Electron. Agric. 215, 108366.

Sahoo, R.N., Rejith, R., Gakhar, S., Verrelst, J., Ranjan, R., Kondraju, T., Meena, M.C., Mukherjee, J., Dass, A., Kumar, S., 2024. Estimation of wheat biophysical variables through UAV hyperspectral remote sensing using machine learning and radiative transfer models. Comput. Electron. Agric. 221, 108942.

Shi, Y., Huang, W., González-Moreno, P., Luke, B., Dong, Y., Zheng, Q., Ma, H., Liu, L., 2018. Wavelet-based rust spectral feature set (WRSFs): a novel spectral feature set based on continuous wavelet transformation for tracking progressive host–pathogen interaction of yellow rust on wheat. Remote Sens 10, 525.

Shuai, L., Li, Z., Chen, Z., Luo, D., Mu, J., 2024. A research review on deep learning combined with hyperspectral imaging in multiscale agricultural sensing. Comput. Electron. Agric. 217, 108577.

Singh, K.D., Duddu, H.S., Vail, S., Parkin, I., Shirtliffe, S.J., 2021. UAV-based hyperspectral imaging technique to estimate canola (Brassica napus L.) seedpods maturity. Can. J. Remote. Sens. 47, 33–47.

Smigaj, M., Gaulton, R., Suárez, J.C., Barr, S.L., 2019. Canopy temperature from an unmanned aerial vehicle as an indicator of tree stress associated with red band needle blight severity. For. Ecol. Manag. 433, 699–708.

Song, L., Cai, J., Wu, K., Li, Y., Hou, G., Du, S., Duan, J., He, L., Guo, T., Feng, W., 2025. Early diagnosis of wheat powdery mildew using solar-induced chlorophyll fluorescence and hyperspectral reflectance. Eur. J. Agron. 162, 127427.

Tagliabue, G., Boschetti, M., Bramati, G., Candiani, G., Colombo, R., Nutini, F., Pompilio, L., Rivera-Caicedo, J.P., Rossi, M., Rossini, M., 2022. Hybrid retrieval of crop traits from multi-temporal PRISMA hyperspectral imagery. ISPRS J. Photogramm. Remote Sens. 187, 362–377.

Tian, L., Xue, B., Wang, Z., Li, D., Yao, X., Cao, Q., Zhu, Y., Cao, W., Cheng, T., 2021. Spectroscopic detection of rice leaf blast infection from asymptomatic to mild stages with integrated machine learning and feature selection. Remote Sens. Environ. 257, 112350.

Vatter, T., Barceló, M., Gjakoni, P., Segarra, G., Trillas, M.I., Aranjuelo, I., Kefauver, S.C., Araus, J.L., 2024. Comparing high-cost and lower-cost remote sensing tools for detecting pre-symptomatic downy mildew (Pseudoperonospora cubensis) infections in cucumbers. Comput. Electron. Agric. 218, 108736.

Verhoef, W., Bach, H., 2007. Coupled soil–leaf-canopy and atmosphere radiative transfer modeling to simulate hyperspectral multi-angular surface reflectance and TOA radiance data. Remote Sens. Environ. 109, 166–182.

Verrelst, J., Rivera-Caicedo, J.P., Reyes-Muñoz, P., Morata, M., Amin, E., Tagliabue, G., Panigada, C., Hank, T., Berger, K., 2021. Mapping landscape canopy nitrogen content from space using PRISMA data. ISPRS J. Photogramm. Remote Sens. 178, 382–395.

Wan, L., Zhang, J., Dong, X., Du, X., Zhu, J., Sun, D., Liu, Y., He, Y., Cen, H., 2021. Unmanned aerial vehicle-based field phenotyping of crop biomass using growth traits retrieved from PROSAIL model. Comput. Electron. Agric. 187, 106304.

Wang, N., Yang, P., Clevers, J.G., Wieneke, S., Kooistra, L., 2023. Decoupling physiological and non-physiological responses of sugar beet to water stress from sun-induced chlorophyll fluorescence. Remote Sens. Environ. 286, 113445.

Wang, J., Zhang, S., Lizaga, I., Zhang, Y., Ge, X., Zhang, Z., Zhang, W., Huang, Q., Hu, Z., 2024a. UAS-based remote sensing for agricultural monitoring: current status and perspectives. Comput. Electron. Agric. 227, 109501.

Wang, Y., Zou, B., Xu, J., Xu, C., Tang, Y.Y., 2024b. ALR-HT: a fast and efficient Lasso regression without hyperparameter tuning. Neural Netw. 106885.

Watt, M.S., Poblete, T., de Silva, D., Estarija, H.J.C., Hartley, R.J., Leonardo, E.M.C., Massam, P., Buddenbaum, H., Zarco-Tejada, P.J., 2023. Prediction of the severity of Dothistroma needle blight in radiata pine using plant based traits and narrow band indices derived from UAV hyperspectral imagery. Agric. For. Meteorol. 330, 109294.

Xiao, Y., Dong, Y., Huang, W., Liu, L., Ma, H., 2021. Wheat fusarium head blight detection using UAV-based spectral and texture features in optimal window size. Remote Sens 13, 2437.

Xiao, D., Pan, Y., Feng, J., Yin, J., Liu, Y., He, L., 2022. Remote sensing detection algorithm for apple fire blight based on UAV multispectral image. Comput. Electron. Agric. 199, 107137.

Zarco-Tejada, P.J., Camino, C., Beck, P., Calderon, R., Hornero, A., Hernández-Clemente, R., Kattenborn, T., Montes-Borrego, M., Susca, L., Morelli, M., 2018. Previsual symptoms of Xylella fastidiosa infection revealed in spectral plant-trait alterations. Nat Plants 4, 432–439.

Zarco-Tejada, P.J., Poblete, T., Camino, C., González-Dugo, V., Calderon, R., Hornero, A., Hernandez-Clemente, R., Román-Écija, M., Velasco-Amo, M.P., Landa, B.B., 2021. Divergent abiotic spectral pathways unravel pathogen stress signals across species. Nat. Commun. 12, 6088.

Zeng, Y., Hao, D., Huete, A., Dechant, B., Berry, J., Chen, J.M., Joiner, J., Frankenberg, C., Bond-Lamberty, B., Ryu, Y., 2022. Optical vegetation indices for monitoring terrestrial ecosystems globally. Nat. Rev. Earth Environ. 3, 477–493.

Zhang, J., Sun, B., Yang, C., Wang, C., You, Y., Zhou, G., Liu, B., Wang, C., Kuai, J., Xie, J., 2022. A novel composite vegetation index including solar-induced chlorophyll fluorescence for seedling rapeseed net photosynthesis rate retrieval. Comput. Electron. Agric. 198, 107031.

Zhang, C., Lane, B., Fernández-Campos, M., Cruz-Sancan, A., Lee, D.-Y., Gongora-Canul, C., Ross, T.J., Da Silva, C.R., Telenko, D.E., Goodwin, S.B., 2023. Monitoring tar spot disease in corn at different canopy and temporal levels using aerial multispectral imaging and machine learning. Front. Plant Sci. 13, 1077403.

Zhao, J., Kang, Z., 2023. Fighting wheat rusts in China: a look back and into the future. Phytopathol. Res. 5, 6.

Zhu, J., Lu, J., Li, W., Wang, Y., Jiang, J., Cheng, T., Zhu, Y., Cao, W., Yao, X., 2023. Estimation of canopy water content for wheat through combining radiative transfer model and machine learning. Field Crop Res. 302, 109077.